High-precision electron-spin sensing with ensembles of nitrogen-vacancy centers in diamond

by

Tamara Đorđević

Submitted to the Department of Physics
in partial fulfillment of the requirements for the degree of

Bachelor of Science in Physics

at the

MASSACHUSETTS INSTITUTE OF TECHNOLOGY

June 2015

Author ... Signature redacted ....
Department of Physics
May 8, 2015

Certified by. Signature redacted ....
Dirk R. Englund
Assistant Professor of Electrical Engineering and Computer Science
Thesis Supervisor

Certified by.. Signature redacted ....
Vladan Vuletić
Professor of Physics
Thesis Supervisor

Accepted by.. Signature redacted ....
Nergis Mavalvala
Chairman, Department Committee on Graduate Theses

High-precision electron-spin sensing with ensembles of nitrogen-vacancy centers in diamond

by

Tamara Đorđević

Submitted to the Department of Physics
on May 8, 2015, in partial fulfillment of the
requirements for the degree of
Bachelor of Science in Physics

Abstract

This thesis describes physical background and an experimental realization of a bulk diamond magnetic field and temperature sensor. The sensing is done using continuous-wave electron-spin resonance spectra of nitrogen-vacancy centers in diamond. Experiments were performed using a light-trapping diamond waveguide sample, with which we estimate to address 10^{13} nitrogen-vacancy centers simultaneously. We derive energy level structure of a nitrogen-vacancy center and recover resonant frequencies of the ESR spectrum. Using the Lindblad master equation, we model ESR lineshape and for the first time consider the influence of infrared driving on the ESR contrast. Both continuous-wave and pulsed sensing protocols are described, and a novel reference-free temperature sensing scheme is proposed. In addition to building a laboratory setup for sensing, we discuss how to miniaturize the setup components and make an on-chip diamond sensor. In particular, we optimize the on-chip fluorescence collection apparatus. Finally, using the built laboratory setup, we demonstrate magnetic field sensitivity floor on the order of 1 $\mathrm{nT/Hz^{1/2}}$ and temperature sensitivity floor of 0.3 $\mathrm{mK/Hz^{1/2}}$.

Thesis Supervisor: Dirk R. Englund
Title: Assistant Professor of Electrical Engineering and Computer Science

Thesis Supervisor: Vladan Vuletić
Title: Professor of Physics

Acknowledgments

I would first like to thank prof. Dirk Englund for providing incessant guidance and mentorship during the two years I worked in the Quantum Photonics Group. He taught me how to independently work on a research project and inspired me to pursue a career in making quantum devices. I would also like to thank prof. Vladan Vuletić for graciously agreeing to co-supervise this thesis.

My research skills greatly improved during the two years in QPG, for which I need to thank its members who never denied me support or help. Most of all I would like to thank Hannah Clevenson, who worked with me on each and every step of the work presented in this thesis. She consistently provided insightful remarks and feedback on all my scientific writing in the last year, while also teaching me many experimental concepts and being a friend outside of lab. I would like to thank MIT's Undergraduate Research Opportunities program which supported me financially in all my research endeavors.

I greatly enjoyed my time at MIT because of many people. Prof. Peter Fisher provided academic support and advising throughout. Prof. David Pritchard was the best junior lab instructor one can hope for. I would not have come to MIT if it were not for my parents and my sister, who always supported my enthusiasm and loved me infinitely, even from afar. Michael Turek kept my head up every day for four years and made me genuinely happy. My gratitude goes to all of them.

One cannot go through MIT without perseverance and love for science. Both of these I got from my first physics professor, Gordana Stanojević. This thesis is dedicated to her and all the professors that change our lives forever.

THIS PAGE INTENTIONALLY LEFT BLANK

Contents

List of Figures

List of Tables

THIS PAGE INTENTIONALLY LEFT BLANK

Chapter 1

Introduction

Quantum physics was developed at the beginning of the 20th century. After more than hundred years of constant research, quantum physics surpassed its initial ambitions of explaining up to then unexplained black body radiation spectrum and atomic structure, and went into predicting new phenomena which can possibly be utilized for various applications. Contemporary quantum physics research therefore aims at not only exploring quantum phenomena, but at exploiting them for practical purposes. The largest research effort in applied quantum physics is directed towards quantum computing. However, isolated (or highly coherent) quantum systems useful for quantum computation are also useful for other applications such as sensing. This thesis is concerned with one of those highly coherent systems - a negatively charged nitrogen-vacancy center in diamond. Specifically, we will present the physical background behind using nitrogen-vacancy centers for magnetic field and temperature sensing, and describe an experimental realization of a bulk diamond sensor.

The nitrogen-vacancy center in diamond is a point defect in the diamond lattice. It consists of a nitrogen and a vacancy next to each other, substituting two carbon atoms, as shown in Figure 1-1. Three carbon atoms (C_1, C_2,C_3), the nitrogen (N) and the vacancy (V) make a unit tetrahedral lattice. In a bulk lattice, $N-V$ orientation may take one out of four possible directions in a tetrahedron. In an ensemble of many NVs, we can generally expect to find all four orientations of NVs. An NV center can be manufactured through various processes such as ion implantation and annealing, and radiation damage and annealing. Improvement of the efficiency and precision of NV fabrication is a vibrant area of research.

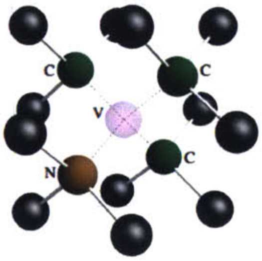

Figure 1-1: Lattice structure of an NV center, adapted from [12]

There are two types of NV centers - a neutral NV center, NV^0, and a negatively charged NV center, NV^-. This thesis, alongside with most current NV research, focuses on NV^-. The electronic structure of an NV^- center consists of six electrons - five from the bonds of a nitrogen and two carbon atoms, and one extra electron accepted from a donor which makes the overall center negatively charged. Based on various studies [12], only two electrons are valence and easily undergo transitions between NV^- energy levels. Therefore, NV^- is a spin 1 system, a fact which will be widely used in further discussion.

Due to its point defect structure, an NV center effectively behaves as a trapped atom-like system in a solid-state lattice. This implies that the energy level structure of an NV has discrete components (like in an atom), which can be separated from continuous conduction and insulation bands characteristic for solids. On the other hand, NVs are stable at the room temperature, and their transitions do not undergo Doppler broadening due to natural carbon-lattice confinement. These properties make NVs attractive for various quantum engineering purposes - they exhibit all the richness of the atomic physics, but are more straightforward to manipulate and, if necessary, integrate into larger systems.

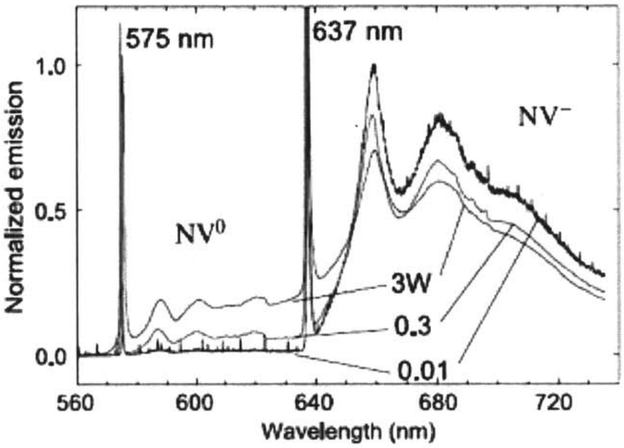

Figure 1-2: Fluorescence spectrum of an ensemble with both NV^0 and NV^- centers, adapted from [12].

The relevant discrete energy levels of an NV^- are shown in the figure 1-3. The following are the most notable characteristics:

1. NV^- has a ground state and first excited state separated by 637 nm. This line, known as the zero phonon line (ZPL), is the sharpest feature in the optical spectrum of an NV^-, and helps us distinguish NV^- from NV^0, whose zero phonon line is at 575 nm. NVs also have a large phonon sideband due to their coupling to the carbon lattice. When we drive ground-to-excited state transition with a laser at a higher energy than the ZPL, the electrons are excited to vibrational levels above the excited state, from which they relax to the excited state. As they decay from the excited to the ground state, many electrons decay to further vibrational levels. We observe this from a fluorescence spectrum of an NV ensemble, shown in Figure 1-2. The sharp peaks in Figure 1-2 correspond to NV^0 and NV^- ZPLs, while the wide sidebands correspond to phonon-mediated transitions. Only around 3.2% of an NV^- emission goes into ZPL [8]. Since we generally want to observe NV^- fluorescence and filter out NV^0, for best results we put longpass filters at the cutoff wavelength even above 637 nm. As we increase the green laser power, some of the NV^- photoconvert into NV^0, as shown in Figure 1-2 (the fluorescence shifts from being mostly above 637 nm to being below it as

we increase the power). Therefore, we want to keep the laser power as low as possible (as it will be discussed in the later chapters, low laser power will also prevent ESR linewidth power broadening and increase our measurement sensitivity).

2. The ground state and the first excited state are triplets (due to spin 1), whose $m_s = \pm 1$ spin projections are separated from the $m_s = 0$ spin projection with a crystal field splitting of $D_{gs} = 2.87$ GHz for the ground state, and $D_{es} = 1.42$ GHz for the excited state.

3. NV$^-$ also has an intersystem crossing side singlet state, but it is ambiguous where exactly it is positioned with respect to the triplet state [12]. Experimental studies show that the electrons in the spin $|1\rangle$ excited state can non-radiatively decay to this singlet state, from which they further decay to spin $|0\rangle$ ground state. In this way, part of the electrons excited to spin $|1\rangle$ state will undergo a "dark" transition to the ground state via the singlet state, and we observe this as a decrease in the fluorescence intensity of an NV. This is the origin of NV's **Optically Detected Magnetic Resonance spectrum (ODMR)** - we can detect the excited state population in spin $|1\rangle$ state through the decrease in the overall NV fluorescence. An example of the NV$^-$ room temperature ODMR spectrum is shown in Figure 1-3. We use ODMR to obtain **Electron Spin Resonance (ESR)** spectra in the following way:

    - We sweep the microwave frequency around 2.87 GHz to resonantly drive the ground state
    - Once we are at the resonance, part of the electron population from $|0\rangle$ will transfer to $|1\rangle$
    - We also drive the ground-to-excited state transition with a laser of wavelength larger than ZPL (usually a green laser at 532 nm); this excites most of the electrons from a ground spin polarization $|0\rangle$ or $|1\rangle$ to the corresponding excited spin polarization
    - Part of the electrons in excited $|1\rangle$ undergo "dark" transition via singlet state

- As a result, we detect fluorescence minima whenever we are resonant with the ground state $|0\rangle$ to $|1\rangle$ transition → this is our ESR spectrum.

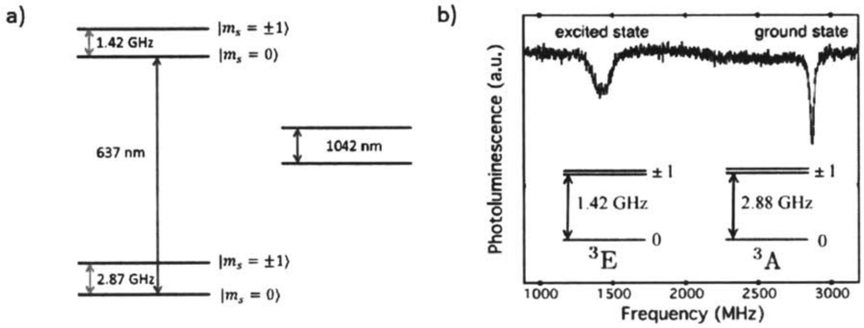

Figure 1-3: a)Sketch of relevant NV^- energy levels and their energy spacing b)An example of NV^- ODMR spectrum at the room temperature, adapted from [12]. Since we are using ground state spin levels for sensing, we only sweep the microwave frequency around 2.87 GHz (peak on the right in the figure).

4. The previously explained decay mechanism of NV^- means that we can deterministically polarize it into $|0\rangle$ ground state. Observations suggest that the polarization can be achieved in a few optical cycles [12]. Since the fluorescence at a time t is proportional to the population of electrons in state $|0\rangle$ at a time t, one can optically read out the population changes in the state $|0\rangle$. This fact is used in the application of pulsed protocols for sensing which rely on reading out time series population in state $|0\rangle$. Optical polarization and read out render NVs potentially suitable for quantum computation; while this is a fascinating area of NV research, this thesis will not go into it since its main theme is NV-based sensing. In addition to being able to initialize NV state, we are also able to make an arbitrary superposition in the $|0\rangle$, $|1\rangle$ basis using microwave pulses of a certain length [12].

5. The most impressive feature of NV^- is its long coherence time - T_2 can be extended to go up to 1.8 ms [12]. This makes NV^- both suitable for quantum computation

since we can perform many single qubit operations within a coherence time, and for quantum sensing since the measurement sensitivities scale as $1/\sqrt{T_2}$, as it will be further explored.

The goal of this thesis is to explore magnetic field and temperature sensing capabilities of an NV^- bulk sample. To do this, we first explore the NV's energy level structure. We derive energy levels of NV ground state, starting from a Hamiltonian accounting for its zero-field splitting. Using perturbation theory, we explore the influences magnetic and electric/strain field have on energy levels. We also discuss empirical studies of how changing temperature affects the NV energy level structure. We then model NV dynamics under constant laser and microwave illumination, eventually deriving ESR shape. Effects of additional infrared illumination are also considered as a way to improve ESR contrast. We then review magnetic field and temperature sensing protocols, discussing the sensitivity limits. This thesis has several theoretical innovations, such as the derivation of the influence of additional infrared driving on the ESR spectrum shape, and a proposal for absolute temperature sensing. To test the sensing capabilities of a bulk diamond, we built an experimental setup described in chapter 5. We also discuss how to make an on-chip NV sensor and propose an apparatus for fluorescence collection. Finally, using the built setup, we demonstrate magnetic field and temperature measurements, report on their sensitivity, and give an outlook on possible improvements.

Chapter 2

NV$^-$ energy levels

2.1 Ground state Hamiltonian

The negatively charged nitrogen-vacancy center has two unpaired spin-$1/2$ electrons, thus having a total spin $S = 1$. The ground state of the NV$^-$ is therefore a degenerate triplet, consisting of three possible projections of S onto the quantization axis (customary taken to be the z-axis): $|m_s = 1\rangle$, $|m_s = 0\rangle$ and $|m_s = -1\rangle$. In this text we will label the triplet states as $|+\rangle$, $|0\rangle$, $|-\rangle$, respectively ($|\pm\rangle$ states here represent spin eigenstates and not the linear combinations of spin eigenstates, as it is used in some texts). In the matrix notation, the triplet states will be the unit vectors, forming a complete three-dimensional orthonormal basis:

$$|+\rangle = \begin{pmatrix} 1 \\ 0 \\ 0 \end{pmatrix}, |0\rangle = \begin{pmatrix} 0 \\ 1 \\ 0 \end{pmatrix}, |-\rangle = \begin{pmatrix} 0 \\ 0 \\ 1 \end{pmatrix} \tag{2.1}$$

In this basis, the spin operators have the following matrix representation:

$$S_x = \frac{\hbar}{\sqrt{2}} \begin{pmatrix} 0 & 1 & 0 \\ 1 & 0 & 1 \\ 0 & 1 & 0 \end{pmatrix}, S_y = \frac{i\hbar}{\sqrt{2}} \begin{pmatrix} 0 & -1 & 0 \\ 1 & 0 & -1 \\ 0 & 1 & 0 \end{pmatrix}, S_z = \hbar \begin{pmatrix} 1 & 0 & 0 \\ 0 & 0 & 0 \\ 0 & 0 & -1 \end{pmatrix} \tag{2.2}$$

The ground state Hamiltonian without any external fields or strain fields of the spin triplet is given by

$$H_0 = D_{gs}S_z^2/\hbar \tag{2.3}$$

where $\hbar D_{gs}$ is the crystal field splitting energy due to the spin-spin interactions of the two electrons in NV$^-$. Since $|+\rangle$, $|0\rangle$ and $|-\rangle$ states are the eigenstates of S_z and therefore S_z^2, our eigenbasis remains the same as in the equation 2.1 (note that unlike in spin-1/2 systems, $S_z^2 \neq 1$ since spin-1 systems are no longer described with Pauli matrices). The associated eigenvalues of H_0 can be found from the action of H_0 on each of the basis states:

$$H_0 \left|0\right\rangle = 0 \left|0\right\rangle \tag{2.4}$$

$$H_0 \left|\pm\right\rangle = \hbar D_{gs} \left|\pm\right\rangle \tag{2.5}$$

Therefore, crystal field splitting Hamiltonian partly breaks the degeneracy of the ground state triplet by lifting the energy of the $|+\rangle$ and $|-\rangle$ states for $\hbar D_{gs}$.

2.2 Influence of the external magnetic field

If we expose NV$^-$ to an external magnetic field $\vec{B}$, the ground state Hamiltonian acquires an additional term:

$$H_B = \mu_0 g \vec{B} \cdot \vec{S}/\hbar \tag{2.6}$$

where μ_0 is the Bohr magneton and g the Lande g factor. If we opearate in the regime where $H_B << H_0$, which is true for all magnetic fields such that $B << \hbar D_{gs}/g\mu_0 = 1000$ G, we can treat H_B as a perturbation to H_0 and apply time-independent perturbation theory to find the corrections to the energy eigenvalues and eigenstates.

The zeroth order energy eigenvalues, found in Eq. 2.4 and Eq. 2.5, are $E_+^{(0)} = E_-^{(0)} = \hbar D_{gs}$ and $E_0^{(0)} = 0$. The first order energy corrections are given by:

$$E_i^{(1)} = \langle i^{(0)}|H_B|i^{(0)}\rangle \tag{2.7}$$

while the first order eigenstate corrections are given by

$$|i^{(1)}\rangle = \sum_{k\neq i} \frac{\langle k^{(0)}|H_B|i^{(0)}\rangle}{E_i^{(0)} - E_k^{(0)}} |k^{(0)}\rangle \tag{2.8}$$

Applying the equations 2.7 and 2.8 and expanding $H_B = \mu_0 g\,(S_x B_x + S_y B_y + S_z B_z)$ we get the first order energy corrections:

$$E_{\pm}^{(1)} = \pm g\mu_0 B_z, E_0^{(1)} = 0 \tag{2.9}$$

and first order eigenstate corrections:

$$|+^{(1)}\rangle = \frac{g\mu_0(B_x + iB_y)}{\sqrt{2}\hbar D_{gs}} |0\rangle \tag{2.10}$$

$$|-^{(1)}\rangle = \frac{g\mu_0(B_x - iB_y)}{\sqrt{2}\hbar D_{gs}} |0\rangle \tag{2.11}$$

$$|0^{(1)}\rangle = \frac{-g\mu_0}{\sqrt{2}\hbar D_{gs}} \left((B_x - iB_y)\,|+\rangle + (B_x + iB_y)\,|-\rangle\right) \tag{2.12}$$

According to Eq. 2.9, B_x and B_y do not influence the energy eigenvalues to first order. To capture their influence, we have to therefore add the second order energy correction. The second order energy correction is given by:

$$E_i^{(2)} = \sum_{k\neq i} \frac{|\,\langle k^{(0)}|H_B|i^{(0)}\rangle\,|^2}{E_i^{(0)} - E_k^{(0)}} \tag{2.13}$$

The second order energy corrections are therefore:

$$E_+^{(2)} = E_-^{(2)} = \frac{\mu_0^2 g^2}{2\hbar D_{gs}}(B_x^2 + B_y^2) = \frac{\mu_0^2 g^2}{2\hbar D_{gs}} B_\perp^2 \tag{2.14}$$

$$E_0^{(2)} = -\frac{\mu_0^2 g^2}{\hbar D_{gs}} B_\perp^2 \tag{2.15}$$

Summing up the corrections to energy eigenvalues, we finally get:

$$E_+ = \hbar D_{gs} + g\mu_0 B_z + \frac{\mu_0^2 g^2}{2\hbar D_{gs}} B_\perp^2 \tag{2.16}$$

$$E_- = \hbar D_{gs} - g\mu_0 B_z + \frac{\mu_0^2 g^2}{2\hbar D_{gs}} B_\perp^2 \tag{2.17}$$

$$E_0 = -\frac{\mu_0^2 g^2}{\hbar D_{gs}} B_\perp^2 \tag{2.18}$$

With an externally applied microwave field we can drive transitions between $|0\rangle$ and $|+\rangle$, with $\omega_+ = \frac{E_+ - E_0}{\hbar}$, and between $|0\rangle$ and $|-\rangle$, with $\omega_- = \frac{E_- - E_0}{\hbar}$. The ESR spectrum will therefore show two resonant frequencies, ω_+ and ω_-, separated by $\Delta\omega = \omega_+ - \omega_- = 2g\mu_0 B_z/\hbar$. Therefore, the transverse magnetic field does not influence the distance between the ESR peaks (to the second order). The peaks will, however, be centered around a different frequency. Without any magnetic field and with only B_z, the peaks will be centered around crystal field splitting frequency, D_{gs}. Additional transverse magnetic field will shift that center to $\omega_c = D_{gs} + \frac{3\mu_0^2 g^2 B_\perp^2}{2\hbar^2 D_{gs}}$.

As shown before, transverse magnetic field will mix $|+\rangle$ and $|-\rangle$ states with $|0\rangle$ and vice versa. Let us define a parameter $\alpha = \frac{g\mu_0}{\hbar D_{gs}}$ for brevity. The new (unnormalized) basis states will then be :

$$|0\rangle' = |0\rangle - \frac{\alpha}{\sqrt{2}} \left((B_x - iB_y) |+\rangle + (B_x + iB_y) |-\rangle \right) \tag{2.19}$$

$$|\pm\rangle' = |\pm\rangle + \frac{\alpha}{\sqrt{2}} (B_x \pm iB_y) |0\rangle \tag{2.20}$$

Since our ground state is now a mixture of different spin components, ODMR will have a reduced contrast once we projectively measure the population in the zero spin state.

2.3 Hyperfine interaction

The presented NV structure split into levels $|0\rangle$ and $|\pm 1\rangle$ arises from NV's fine structure. For a more precise treatment of energy levels we need to include the interactions between electrons in an NV and surrounding nuclei. This interaction is known as the hyperfine interaction. If a nucleus has an angular momentum I (in the case of a nucleus, this has to be spin angular momentum) and electrons have a total angular momentum J (including both spin and orbital angular momentum), the two momenta will in general interact in the form of $H_{hf} = A\vec{J} \cdot \vec{I}$, where A is the hyperfine interaction constant, empirically measurable for different energy levels. In the case of the ground state NV, $J = S$ since orbital momentum $L = 0$. If we also include the nuclear quadrupole interaction P, the Hamiltonian takes the form:

$$H_{hf} = A_{||}S_zI_z + A_{\perp}(S_xI_x + S_yI_y) + A_{\perp}PI_z^2 \tag{2.21}$$

where the measured values for an NV$^-$ are $A_{||} = -2.14$ MHz, $A_{\perp} = -2.70$ MHz and $P = -5.01$ MHz [14].

In order to continue the analysis, we must determine which nuclei the NV interacts with. The carbon isotope ^{12}C found in NV diamond lattice has nuclear spin zero, so it does not couple to the electron spin. The most prevalent nitrogen isotope ^{14}N has nuclear spin $I = 1$, so this is our dominant source of hyperfine coupling [14]. There are other nuclear spins an NV can couple to which are less prevalent. One of them is the nitrogen isotope ^{15}N which has spin 1/2, resulting in D_{gs} splitting into two resonant frequencies split by 3.05 MHz [23]. The other is the carbon isotope ^{13}C which also has spin 1/2. The splitting strength from ^{13}C depends on the distance of this isotope from the NV center - for different distances, it was measured to be between 8.9 and 12.8 MHz [24]. We do not observe hyperfine splittings due to ^{13}C and ^{15}N in our spectra so we will not consider them in this thesis.

The resulting energy level splittings arising from the interaction with ^{14}N are shown in Figure 2-1. While we do not go through the entire derivation, we can quickly check the number of expected energy levels. The total angular momentum is now given by $\vec{F} = \vec{S} + \vec{I}$. The allowed values for F are $F \in [0, 1, 2]$ ($|I - S| \leq F \leq |I + S|$), and the allowed projections onto the quantization axis are $m_F \in [0, \pm1, \pm2]$, so we expect five m_F levels, as shown in Fig. 2-1. Since $m_F = m_s + m_I$, we can also deduce which eigenstates $|m_s, m_I\rangle$ go into superpositions making joint eigenstates $|m_F\rangle$. The eigenstates are given by:

$$|m_F = 2\rangle = |1,1\rangle \tag{2.22}$$

$$|m_F = -2\rangle = |-1,-1\rangle \tag{2.23}$$

$$|m_F = 1\rangle = (|1,0\rangle + |0,1\rangle)/\sqrt{2} \tag{2.24}$$

$$|m_F = -1\rangle = (|-1,0\rangle + |0,-1\rangle)/\sqrt{2} \tag{2.25}$$

while the eigenstate $|m_F = 0\rangle$ is given by a superposition of states $|0,0\rangle$, $|-1,1\rangle$ and $|1,-1\rangle$ whose weights cannot be determined solely based on symmetry considerations.

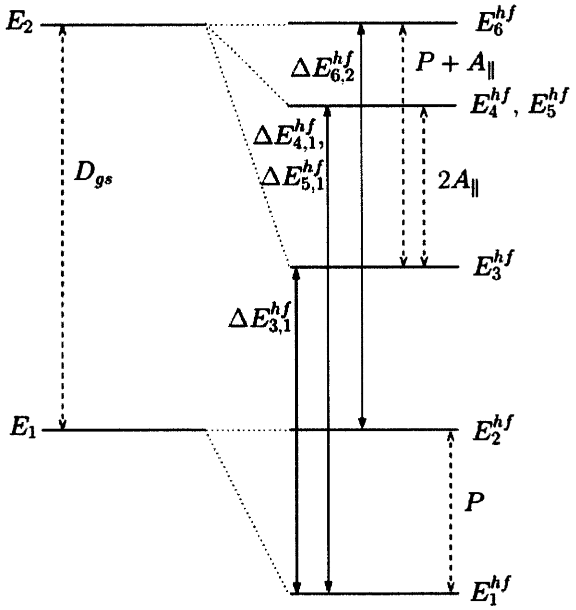

Figure 2-1: ^{14}N hyperfine levels of an NV$^-$, adapted from [14]. The solid arrows indicate allowed magnetic transitions. We expect three transitions of the energies D_{gs}, $D_{gs} - A_{\|}$ and $D_{gs} + A_{\|}$.

We now want to explore what effects will hyperfine interaction have on our ESR spectrum. Based on the Fig. 2-1, both $|+1\rangle$ and $|-1\rangle$ resonances will be split into three subresonances, shifted by $\omega_{hfs} \in [0, A_{\|}, -A_{\|}]$ from $\omega_{\pm}$. We can therefore summarize the influence of the hyperfine splittings as adding $\pm A_{||} m_I$ term to $\omega_\pm$.

It may seem unusual that the hyperfine splittings do not couple to the magnetic field (i.e. we have no terms of the order of $I \cdot B$). This is not strictly correct - in principle we should add a term proportional to $g_N \mu_N \vec{I} \cdot \vec{B}$ to the total Hamiltonian, where μ_N is the nuclear magnetic moment and g_N nuclear Lande factor. The Lande g factor is given by $g_N = 0.4035$ for nitrogen ^{14}N [14], while nuclear magnetic moment is equal to $\mu_N \approx 5 \times 10^{-27}$ J/T, a value 10^4 times smaller than the electron magnetic moment μ_e. Due to μ_e being much larger than μ_N, which arises from the fact that an electron is $\approx 10^4$ times lighter than a proton, the magnetic interaction between the nucleus and the external field is 10000 times weaker than the Zeeman splitting discussed before. The point where we should include this interaction in our Hamiltonian is when the external field is strong enough that $\mu_N B \approx h A_{||}$, which is at $B \approx 1$ T $= 10000$ G. Since the fields used in this thesis and in NV experiments in general are around hundred times weaker than this limit, we approximate that only electrons interact with the magnetic field.

2.4 Influence of the strain/electric field

Previous studies showed that electric field and crystal strain field can be together treated as a local electric field since their Hamiltonians have equivalent terms [15]. This equivalence can be conceptually understood in the following way. The electric field changes the overlap of electronic wavefunctions by polarizing the charge distributions. The strain field can be understood as an external pressure; pressure also changes the overlap of electronic wavefunctions by mechanically bringing the electrons closer to each other. If we define σ to be the local electric field, we can write the total electric field/strain Hamiltonian as:

$$H_S = d_{||} \sigma_z S_z^2 + d_\perp \sigma_x \left(S_x S_y + S_y S_x \right) + d_\perp \sigma_y \left(S_x^2 - S_y^2 \right) \tag{2.26}$$

where $d_{||}$ and $d_\perp$ are parallel and perpendicular components of the electric dipole moment of the NV$^-$, and σ_i the component of the local electric field in the i direction [15]. The first order corrections to the energy eigenvalues are no longer given by Eq. 2.9, since the degenerate states $|\pm\rangle$ have cross-terms in the matrix representation. The energy corrections are instead obtained by the diagonalization of H_S. The obtained values are:

$$E_0^{(1)} = 0 \tag{2.27}$$

$$E_\pm^{(1)} = d_{||}\sigma_z\hbar^2 \pm d_\perp\hbar^2\sqrt{\sigma_x^2 + \sigma_y^2} = d_{||}\sigma_z\hbar^2 \pm d_\perp\hbar^2\sigma_\perp \tag{2.28}$$

The strength of this interaction is determined by the values of $d_{||}/h = 0.35$ Hz cm/V and $d_\perp/h = 17$ Hz cm/V [15]. If we would want to measure electric field using NVs, it would be more efficient to measure the perpendicular component causing ESR splittings in the same way as measuring B_z since $d_\perp$ is around fifty times larger than $d_{||}$. For the sake of comparison, in order to get a 1 kHz ESR splitting due to perpendicular field, we would need $E_\perp = 60$ V/cm, while for 1 kHz ESR ω_c drift we would need $E_{||} = 2860$ V/cm. This field is achievable, but very high (the electric field needed to cause the air to break down and conduct electricity is $E \approx 10^4$ V/cm, only about five times larger).

While NVs are better suited for measuring the magnetic field than the electric field, it is important to understand how σ affects energy levels to optimize ESR signal. Namely, every diamond sample will have an inherent internal strain field which is likely to be inhomogeneous due to imperfections in diamond growth. These local strain inhomogeneities will cause the ESR linewidths to broaden, so it may be worth characterizing sample's internal strain before using it for sensing. On the other hand, a controlled anisotropic strain could change D_{gs} for different NV orientations, as will be further discussed in chapter 4. This phenomenon could be used for absolute temperature sensing, as well as for improved diamond clock stability [19].

2.5 Temperature drift

The last external influence we consider in this thesis is temperature change. Temperature cannot be treated in the same way as the magnetic and electric fields since there is no

Chapter 3

ESR lineshape

Magnetic field, electric field, strain and temperature sensing are all done using electron-spin-resonance technique (ESR), so it is important to understand the properties of the lineshape of the ESR. Moreover, optimizing ESR contrast (or more specifically, signal-to-noise ratio) increases the sensitivity of the NV quantum sensor. In short, we want to maximize the ESR contrast and minimize the ESR linewidth. Therefore, the purpose of this chapter is to derive the lineshape of the NV induced ESR and apply the derived result to the optimization of the ESR contrast, leading to a better signal-to-noise ratio and thus better sensitivity for magnetometry and thermometry.

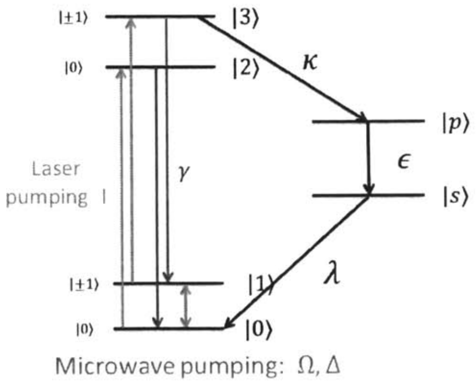

Figure 3-1: Level diagram of NV$^-$ with relevant decay and pumping rates. The laser pumping rate I, Rabi frequency Ω and detuning from resonance Δ of the microwave excitation can be controlled by the experimental setup. The decay rates $\gamma = 1/10\ \mathrm{ns}^{-1}$, $\kappa = 1/30\ \mathrm{ns}^{-1}$, $\epsilon = 1/0.9\ \mathrm{ns}^{-1}$ and $\lambda = 1/300\ \mathrm{ns}^{-1}$ are internal characteristics of the NV$^-$, whose values are adapted from [12].

Following the procedure used in [19] the internal NV$^-$ dynamics can be described using the Lindblad master equation:

$$\dot{\rho} = -\frac{i}{\hbar}[H,\rho] + \sum_k \left(L_k \rho L_k^\dagger - \frac{1}{2} L_k^\dagger L_k \rho - \frac{1}{2} \rho L_k^\dagger L_k \right) \tag{3.1}$$

where ρ is the 6×6 density matrix associated with the NV$^-$ states, H is the NV Hamiltonian and L_k are jump operators associated with the transitions taken into consideration. The relevant transitions and their rates are shown in Figure 3-1. We neglect the spin flip and dephasing rates, as well as deshelving from the ground to the excited state (i.e. we take that all electrons from spin $|0\rangle$ ground state are pumped to the spin $|0\rangle$ excited state, and none to spin $|1\rangle$ excited state). The jump operators are then given by:

$$L_1 = \sqrt{I}\,|2\rangle\langle 0|\,, L_2 = \sqrt{I}\,|3\rangle\langle 0|\,, L_3 = \sqrt{\kappa}\,|p\rangle\langle 3|\,, L_4 = \sqrt{\lambda}\,|0\rangle\langle s|\,,$$

$$L_5 = \sqrt{\gamma}\,|0\rangle\langle 2|\,, L_6 = \sqrt{\gamma}\,|1\rangle\langle 3|\,, L_7 = \sqrt{\epsilon}\,|s\rangle\langle p|$$

For simplicity, we will start by solving for the populations of the dark states $|p\rangle$ and $|s\rangle$.

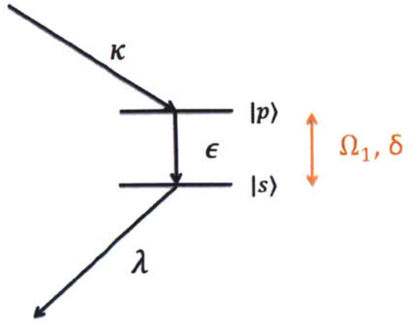

Figure 3-2: Level diagram of NV$^-$ dark states.

The level diagram of the dark states is shown in the figure 3-2. The transition from $|p\rangle$ to $|s\rangle$ level is in the infrared domain, with a ZPL of 1042 nm. Theoretically, we could pump that transition as well in order to "slow down" the decay time from $|s\rangle$ to $|0\rangle$. In this section, we will analyze the most general case in which we pump this transition with a Rabi frequency Ω_1, detuned by δ from the resonance. The Hamiltonian for the dark states is then given by

$$h_d = \delta\left(|p\rangle\langle p| - |s\rangle\langle s|\right) + \Omega_1\left(|p\rangle\langle s| + |s\rangle\langle p|\right) \tag{3.2}$$

Using this Hamiltonian and equation 3.1, and solving for the steady state populations ($\dot{\rho} = 0$), we get the following populations (expressed in terms of diagonal elements of ρ):

$$\rho_{ss} = \frac{\kappa}{\lambda}\rho_{33} \tag{3.3}$$

$$\rho_{pp} = \rho_{ss}\frac{\Omega_1^2(\lambda+\epsilon) + \lambda(4\delta^2 + (\lambda+\epsilon)^2/4)}{\Omega_1^2(\lambda+\epsilon) + \epsilon(4\delta^2 + (\lambda+\epsilon)^2/4)} \tag{3.4}$$

Without pumping, $\rho_{pp} = \rho_{ss}\frac{\lambda}{\epsilon}$, which goes to zero if $\epsilon >> \lambda$. This recovers the result from [19] which neglects the level $|p\rangle$ altogether. However, in the case of pumping, the population in ρ_{pp} cannot be neglected since Ω_1^2 approaches quadratically to ϵ. For brevity, we can re-express equation 3.4 as $\rho_{pp} = f\rho_{ss}$, so that $f/(1+f)$ electrons transfer from ρ_{ss} to ρ_{pp} due to the pumping. The maximal value of f is $f = 1$, which corresponds to half the population transferred from $|s\rangle$ to $|p\rangle$. Some of the plots of the dependence of f on δ and Ω_1 are shown in Figure 3-3.

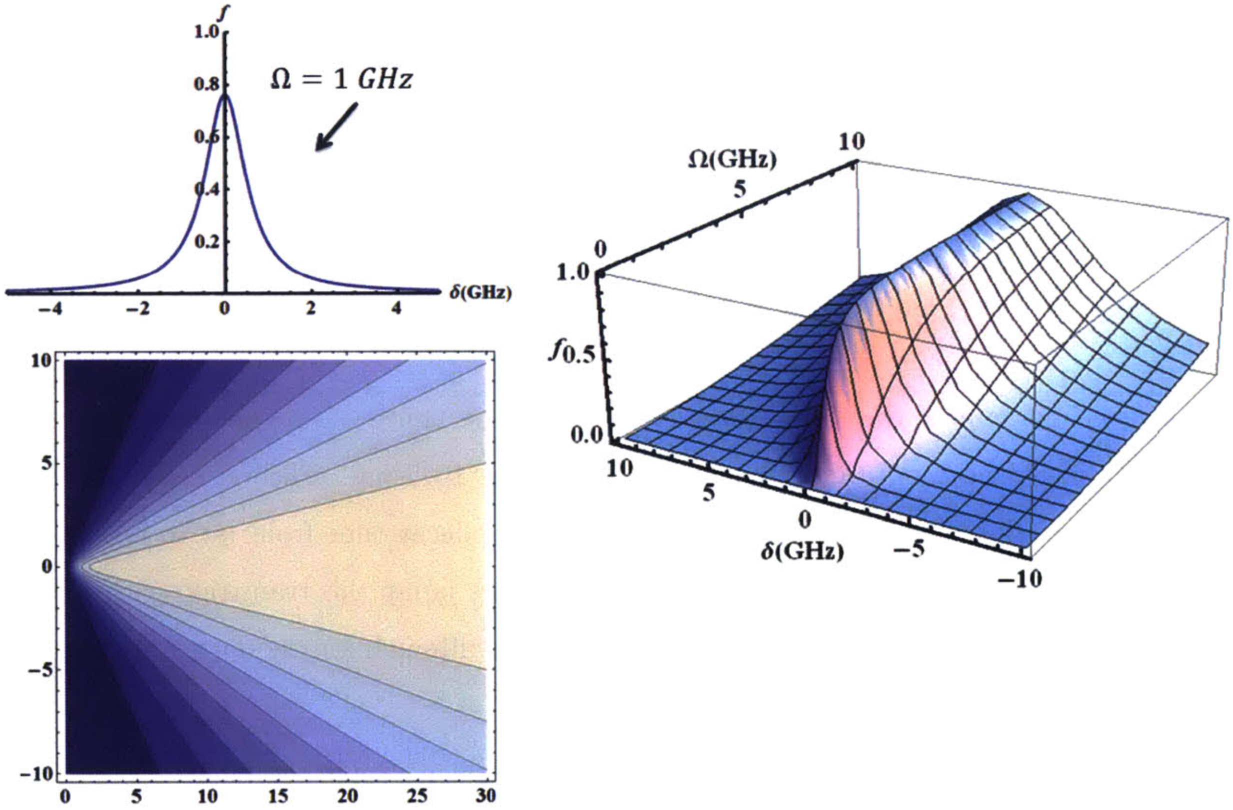

Figure 3-3: (Left)Dependence of the f parameter on the detuning δ from the transition (x axis) and pump strength Ω_1 (y axis); (Right up) A slice of a constant Rabi frequency showing the strong dependence of f on the detuning; (Right down) Contour plot of f versus detuning (y axis) and Rabi frequency (x axis).

Figure 3-3 shows different ways in which we can achieve high f values - we can decrease the detuning from the resonant frequency or increase our coupling strength (Rabi frequency). An experimentally more useful figure of merit would be allowed detuning in terms of nanometers from the 1042 nm resonance which would still achieve high f. The dependence of f on nanometer detuning is thus given in Figure 3-4. We see that f depends very strongly on the detuning, and that we would need to lock our laser to within 1 pm of the transition wavelength in order to achieve high f.

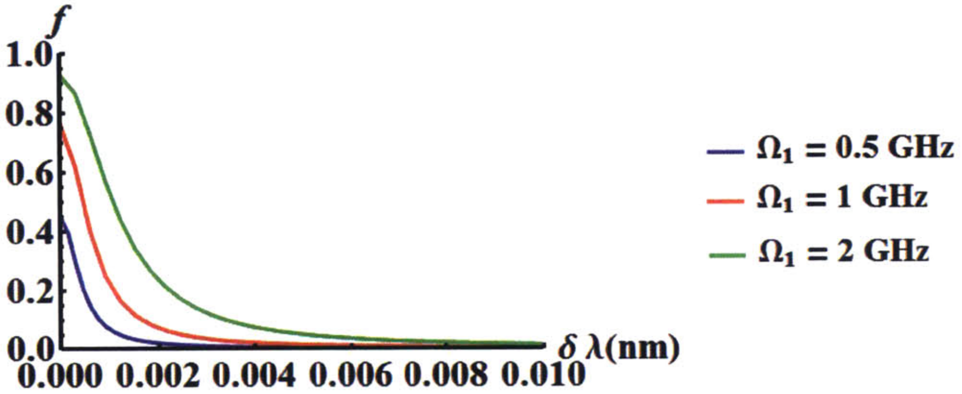

Figure 3-4: Dependence of the f parameter on the detuning $\delta\lambda$ from the transition wavelength of 1042 nm for different values of Rabi frequency Ω_1

We find the rest of the density matrix elements by applying the Lindbland equation (3.1) to the ground state Hamiltonian:

$$H_{gs} = \Delta\left(|1\rangle\langle 1| - |0\rangle\langle 0|\right) + \Omega\left(|1\rangle\langle 0| + |0\rangle\langle 1|\right) \tag{3.5}$$

where Δ and Ω are detuning and Rabi frequency of the ground state, respectively. We can control Δ and Ω by controlling the power, frequency and alignment of the microwave excitation source in our setup.

We obtain the excited state populations to be

$$\rho_{22} = \frac{I}{\gamma}\rho_{00} \tag{3.6}$$

$$\rho_{33} = \frac{I}{\gamma+\kappa}\rho_{11} \tag{3.7}$$

In calculating the excited state populations we neglect off-diagonal matrix elements of the excited states since they decay much faster than the other elements [19]. The calculation of the ground state populations is more involved since we cannot neglect off-diagonal elements because we are driving the ground state with an external field that mixes its sublevels. We obtain the following equations and set them to zero to obtain steady-state populations:

$$\begin{aligned}
\dot{\rho}_{00} &= i\Omega(\rho_{10} - \rho_{01}) - I\rho_{00} + \lambda\rho_{ss} + \gamma\rho_{22} \\
\dot{\rho}_{11} &= -i\Omega(\rho_{10} - \rho_{01}) - I\rho_{11} + \gamma\rho_{33} \\
\dot{\rho}_{01} &= -2i\Delta\rho_{01} + i\Omega(\rho_{11} - \rho_{00}) - I\rho_{01} \\
\dot{\rho}_{10} &= 2i\Delta\rho_{10} - i\Omega(\rho_{11} - \rho_{00}) - I\rho_{10}
\end{aligned}$$

Finally, to normalize the populations in different states, we use the condition that $tr[\rho] = 1$ and extract each ρ_{ii} as a dimensionless parameter (exact formulas omitted from the text due to length).

Our fluorescence signal comes from the decay from excited states ($|2\rangle$ and $|3\rangle$) to the ground states ($|0\rangle$ and $|1\rangle$). Therefore, we can model fluorescence signal as [19] :

$$F(\Delta, f) = \gamma\left(\rho_{22}(\Delta, f) + \frac{\gamma}{\gamma+\kappa}\rho_{33}(\Delta, f)\right) \tag{3.8}$$

Since the laser pump frequency I, microwave Rabi frequency Ω and f (related to infrared laser Rabi frequency Ω_1 and detuning δ) are the free parameters of our experiments, we want to investigate how they affect the NV ESR lineshape. We look into each one of them separately:

1. **Laser power I:** Higher laser power will in general give more fluorescence signal because we can address more NVs in a bulk sample at the same time. However, if we are looking at a single NV, we expect higher laser power to cause power broadening of the ESR line.

   In order to separate the influence of I, we plot $F(\Delta, f)$ for $f = 0$, Rabi frequency fixed at $\Omega = 10$ GHz, and three different values of $I \in \{10, 50, 100\}$ GHz. The plot is shown in Figure 3-5. From the plot we can see that higher laser powers cause both line broadening and decrease the contrast. Therefore, for addressing a single NV, we should decrease the laser power as much as possible.

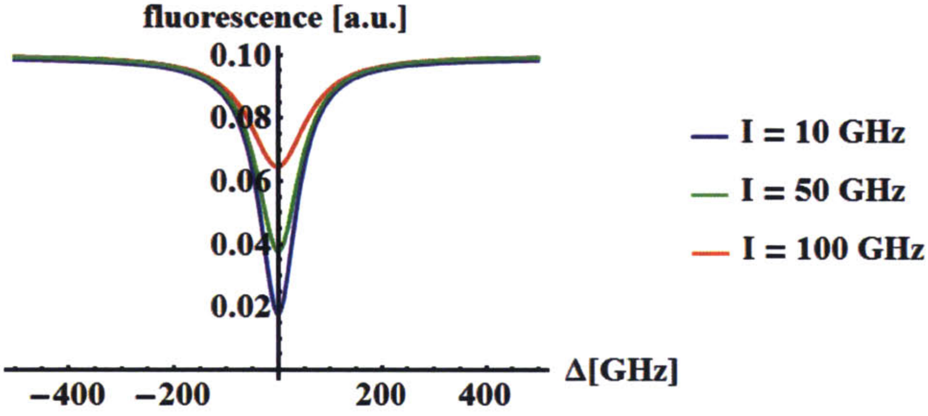

Figure 3-5: Dependence of the ESR lineshape on the laser pump power I

2. **Microwave power Ω:** We plot $F(\Delta, f)$ for $f = 0$, fixed $I = 10$ GHz and four different values of $\Omega \in \{1, 10, 50, 100\}$ GHz. The plot is shown in Figure 3-6. We notice that higher Ω causes line broadening, while its effect on the contrast is more ambiguous. The increase of Ω from 1 GHz to 10 GHz improves the contrast, but further increase has no effect. Additionally, line broadening effects are much stronger for Ω than for I.

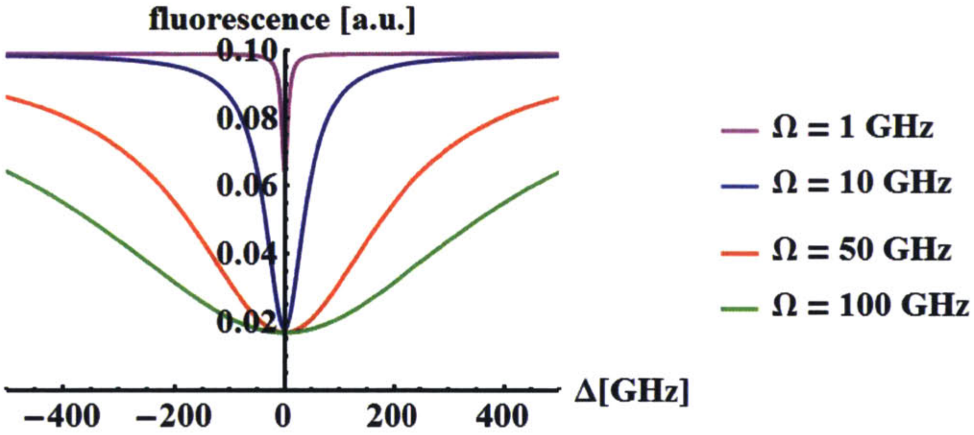

Figure 3-6: Dependence of the ESR lineshape on the microwave pump power Ω

3. **Dark state driving f:** The influence of the f parameter on the ESR lineshape is

ambiguous since we both expect it to broaden the line and to increase the contrast. We plot $F(\Delta, f)$ for fixed $I = 10$ GHz, $\Omega = 10$ GHz, and $f \in \{0, 0.5, 1\}$ in Figure 3-7. We see that higher f both causes line broadening and contrast improvement, as predicted.

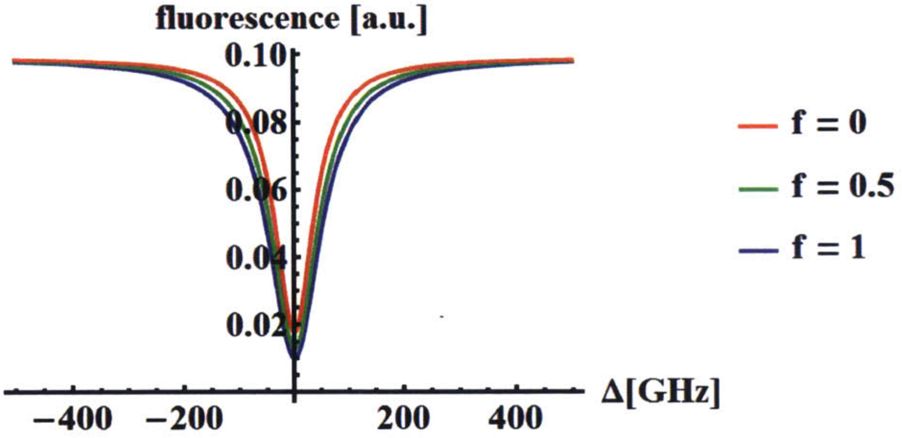

Figure 3-7: Dependence of the ESR lineshape on the dark state pumping through the parameter f

We can now compare results obtained in previous derivations with the empirical results reported in Ref. [17]. Ref. [17] reports that linewidth monotonically increases and contrast monotonically decreases as we increase the laser power, which is consistent with our prediction. The influence of Ω is also consistent with our calculations. Higher Ω increases the linewidth as predicted, but it also improves the contrast. The contrast improvement levels out after we reach saturation, after which the contrast stays constant. The point where the contrast levels out depends on the laser power as well, but for the powers used in the study, the contrast would level out at around 0.01 GHz. Our contrast levels out between 1 and 10 GHz, which implies that the laser power of 10 GHz used for this estimation is higher than the laser power used in Ref. [17]. Overall, our modeling of ESR dynamics matches all the predictions from empirical studies in terms of laser and microwave power influences. Therefore, we believe that the predicted influence of the infrared driving would be also matched to empirical results should anyone consider using this technique.

Chapter 4

Sensing applications

Our diamond sensing setup can independently measure $\Delta\omega$ and ω_c given by equations 2.31 and 2.30. We use $\Delta\omega$ to measure B_z and ω_c to measure temperature. In this chapter we present an overview of magnetic field and temperature sensing techniques, as well as protocols that can be used for NV-based sensing. While our experiments were done using continuous-wave excitation protocols, we present pulsed protocols as well for completeness. Finally, we discuss sensitivity limits of the envisioned diamond sensor.

4.1 Magnetic field sensing

4.1.1 Overview

Sensitive measurements of magnetic field are important for many applications such as geomagnetics and biosensing. NV center based magnetometers are inspired by the atomic magnetometers which date far before the discovery of NV centers. Some of the earliest work in atomic vapor magnetometry was done by Dehmelt, Bell and Bloom in 1957 [9]. Atomic vapor magnetometry uses a resonant laser field which puts the spin states in a superposition; the superposition evolves due to Larmor precession in the external magnetic field and changes the absorption properties of atoms; magnetic field is read-off by detecting transmitted light through the atomic vapor [9]. Atomic vapor cells are still being perfected - one of the most sensitive atomic vapor magnetometers currently reaches sensitivity of 1 fT/Hz$^{1/2}$ in the frequency band of $10 - 150$ Hz [20]. Similar sensitivity in the low frequency range is reached with SQUID magnetometers.

There are a couple of figures of merit that should be taken into consideration when one evaluates the usefulness of a magnetometer. One of them is the aforementioned sensitivity and the frequency band over which it can be reached. One can also ask if the measured quantity is a scalar or a vector, i.e. if we can determine the direction of the magnetic field as well as its magnitude. Additionally, spatial resolution (usually equal to the size of the sensing sample) of a magnetometer is very important for its applications. Finally, the complexity of the setup needed for sensing limits many of the possible practical applications. This is especially true if the sensor needs to operate at cryogenic temperatures, in which case the sensor is less portable and more expensive.

NV-center-based magnetometry is derived from the atomic magnetometry in that it exploits the behavior of discrete energy levels in an external field. The magnetic field can be extrapolated by either measuring the energy level shifts caused by the Zeeman effect or by measuring the electron population transfer due to Larmor precession. Atomic vapor cells are improved by extending the number of addressed atoms in the vapor. Similarly, in bulk diamond we improve the sensitivity by increasing the number of addressed NVs. As it will be further discussed in chapter 5, this thesis uses a light-trapping diamond waveguide as an NV sample, with which we estimate to address $N \approx 10^{13}$ NVs simultaneously. As a comparison, atomic vapor cells are reported to address $10^{11} - 10^{15}$ atoms, while trapped ultracold atom setups can simultaneously use around $10^{6} - 10^{8}$ atoms [9].

While atomic vapor cells and SQUIDs have so far demonstrated higher sensitivity than NV based sensors in the low frequency range, NVs may offer some competitive figures of merit. For one, a bulk NV sample can be used to determine the direction of the magnetic field vector since we measure magnetic field projections onto four diamond axes. Atomic vapor cells do not have this ability, since atoms in Brownian motion do not have preferential directions. Atomic vapor cells have spatial resolution on the order of a couple of mm (the size of a vapor cell) [9]. Bulk NV sample used in this thesis has a similar spatial resolution (3 mm), but single NVs have also been used for sensing, in which case the resolution goes all the way to a nm [?]. Both atomic vapor cells and NVs operate at room temperature, which means that their sensing setups can be significantly miniaturized. Building on this fact, in this thesis we explore some of the ways we could make an on-chip diamond sensor.

Some of the main applications of high-precision magnetic field sensing are in biosensing, including the detection of fields present in the heart and brain [9]. One of the most attractive applications for high-precision magnetometry is magnetoencephalography, in which we try to connect different brain functions with different magnetic field distributions, thus identifying the particular regions of the brain used for activities such as visual or auditory processing. So far, magnetoencephalography has been done with SQUIDs, but SQUIDs do not promise to reach wider audience for this purpose since the cryogenic setups are very cost-inefficient. Both atomic vapor cells and NVs are good candidates to replace SQUIDs in magnetoencephalography. Another advantage of NVs over all other platforms is that diamond is bio-compatible, i.e. we could in principle inject nanodiamonds with NVs into living tissue without disturbing it. This method was used for NV based thermometry in a living cell, as it will be further discussed, but it could be also used for in-vivo magnetic field measurement [21].

4.1.2 Continuous wave protocols

All the experiments presented in this thesis were done using a continuous wave (CW) excitation by both the laser and the microwave field. CW sensing measures magnetic field by measuring the Zeeman shifted energies in the ESR spectrum, as explained in the previous sections. The upside of a CW measurement is that it needs only one frequency sweep to determine magnetic field, while Ramsey-type pulsed protocols need repetitive measurements to obtain statistics about the electron population, as it will be discussed below. The downside of a CW measurement is that it is prone to linewidth broadening which affects the measurement sensitivity. Some of those effects were explored in chapter 3. Pulsed protocols, on the other hand, do not suffer from linewidth broadening since the system is pulsed with a single resonant frequency (there are other broadening mechanisms for pulsed protocols such as lifetime broadening, however, we do not explore them in this thesis). The pulse shape imperfections, however, effectively shorten the NV coherence times, thus reducing the sensitivity.

To the author's best knowledge, the only CW NV sensing protocol different from the one used in this thesis is by CW infrared absorption [5]. In this method, the authors use an additional CW illumination by the 1042 nm laser which is absorbed if there are electrons in the dark state discussed in chapter 3. Since electrons only transfer to the dark state if they are polarized in $|\pm\rangle$ spin states, we see a dip in transmission each time we are resonant with the ground state transition. Therefore, if we measure the IR laser transmission versus the microwave frequency, we obtain ESR spectra completely equivalent to those used in this thesis, with the difference that the contrast can be theoretically better. With this method, Acosta et. al. demonstrated magnetic field sensitivity of 10 $\mathrm{nT/Hz^{1/2}}$ in the frequency range from DC to 140 Hz [5].

4.1.3 Pulsed protocols

Pulsed protocols measure the change in electron population due to Larmor precession in the external magnetic field. Pulsed protocols are much more versatile than CW since there are many pulse sequences which are used to extend coherence times in parallel with sensing. For example, Aiello et. al. use pulse sequences that improve sensitivity to periodic fields, but which cannot be applied to static or aperiodic fields [7]. Cooper et. al. use Walsh sequences to reconstruct a time-varying field of an unknown shape [11]. Even though versatile, pulsed protocols are all based on the Ramsey pulse sequence. We will therefore describe the Ramsey sequence, and one of its most common extensions, spin-echo refocusing sequence.

A Ramsey pulse sequence is used for DC magnetometry [22]. The sequence proceeds as follows. We first polarize the NV into $|0\rangle$ state with a green laser pulse. Then, we preform a $\pi/2$ microwave pulse which puts the NV into a superposition of $|0\rangle$ and one of the excited states, $|+\rangle$ or $|-\rangle$ (let us choose $|+\rangle$ in this example). After a free evolution time τ, the state becomes

$$(|0\rangle + e^{-ig\mu_0 B_z \tau/\hbar}|+\rangle)/\sqrt{2}$$

After performing another $\pi/2$ pulse, we project the phase difference into the population difference of the state $|0\rangle$. After reading off the population in $|0\rangle$ with a green laser pulse, we obtain fluorescence signal proportional to $(1 + \cos(g\mu_0 B_z \tau/\hbar))/2$. Therefore, after repeating this experiment for different values of τ we obtain an oscillatory signal, whose frequency is proportional to the magnetic field B_z.

Spin-echo sequence is the same as Ramsey sequence with the addition of a 2π pulse in the middle of two free time evolutions τ. This pulse is equivalent to a π pulse in a spin 1/2 system. The goal of this pulse is to cancel out spin-dephasing processes since it refocuses spins that lost coherence after time τ. This method cannot be used for DC magnetometry since it also cancels out all the constant B_z phase dependence, but can be used for AC magnetometry if the timing of the 2π pulse coincides with a magnetic field node [22]. If we again vary free time evolution τ and repeat the experiment, we will observe an oscillatory signal with frequency proportional to magnetic field magnitude.

4.1.4 Sensitivity limit of a magnetic field sensor

The fundamental limit on the smallest measurable magnetic field can be estimated from time-energy uncertainty relation:

$$\Delta E \Delta t \geq \frac{\hbar}{2} \tag{4.1}$$

The energy splitting in an external magnetic field is given by $\Delta E = g\mu_0 B$, up to a numerical constant. Since we are looking for an order of magnitude estimate, we can neglect the numerical factors of the order unity and re-express equation 4.1 as

$$\delta B \approx \frac{\hbar}{g\mu_0 \Delta t} \tag{4.2}$$

We can substitute Δt with different spin coherence times based on the method used. DC Ramsey pulsed magnetometry is limited by the spin dephasing time T_2^* so $\Delta t = T_2^*$. AC pulsed magnetometry cancels out spin dephasing processes but is still limited by spin coherence time T_2. Coherence times heavily depend on the quality of the sample and abundance of different carbon and nitrogen isotopes. In general, T_2^* can range from $0.18 - 1\mu$s, T_2 is on the order of 600μs and T_1 is on the order of 6μs [22]. As already mentioned, different pulse sequences can be designed to extend these times. CW magnetometry, as performed in this thesis, is limited by T_2^* which was measured to be $T_2^* = 1\mu$s [10]. Therefore, in further discussion we will replace $\Delta t = T_2^*$.

If we interrogate N NVs within each coherence time (which is the case in a bulk diamond sensor with N NVs addressed at the same time), the sensitivity limit is increased $\sqrt{N}$ times. This increase in sensitivity follows from the central limit theorem, which states that the standard deviation σ of a Gaussian variable is reduced to $\sigma/\sqrt{N}$ after N measurements. Additionally, if we interrogate ensemble of N NVs k times in a row and average out the outcome, the sensitivity improves for an additional factor of $\sqrt{k}$. If we label the integration time as τ, k can be expressed as $k = \tau/T_2^*$. We can now rewrite the equation 4.2 as

$$\delta B \approx \frac{\hbar}{g\mu_0 T_2^* \sqrt{N}\sqrt{k}} = \frac{\hbar}{g\mu_0 T_2^* \sqrt{N}\sqrt{\tau/T_2^*}} = \frac{\hbar}{g\mu_0 \sqrt{N}\sqrt{T_2^* \tau}} \tag{4.3}$$

This fundamental limit on the magnetic sensitivity of a bulk sensor is consistent with the one derived in Ref. [9]. This limit obviously assumes perfect contrast and collection efficiency, so for the practical purposes δB will be adjusted for experimental parameters. In general, the sensitivity scales as $1/C$, where C is the contrast [21].

4.2 Temperature sensing

NV^- centers are used as thermometers by exploiting their dependence of ω_c on temperature. We can in general model ω_c as

$$\omega_c = \omega_{ref} + c(T - T_{ref}) \tag{4.4}$$

where c is a constant equal to $c = \frac{\partial \omega_c}{\partial T}$. Assuming that our perpendicular magnetic field and axial strain are negligible (or that $B_\perp$ is at least negligible at the second order), the entire drift comes from temperature drift of D_{gs}, $c = dD_{gs}/dT = -74$ kHz/K. The temperature measurement studies done so far used these assumptions and measured T based on the zero field splitting drift [27, 21, 10]. Temperature was measured both by using pulsed and continuous wave protocols. In this thesis, we propose an extension of the presented methods to absolute temperature sensing. Namely, previous methods measure temperature after determining ω_{ref} and T_{ref}. These values can in general drift. The goal of an absolute temperature sensor is to eliminate the possibility of the drift by exploiting a stable point of the sample's temperature response.

Since absolute temperature sensing protocols are based on parallel temperature sensing procedures on two different types of NVs, we will present only absolute temperature sensing schemes as a more general result. Methods for regular temperature sensing can be inferred just by neglecting one of the NV populations.

4.2.1 Absolute temperature sensing

In an ensemble of NV centers, we can have four orientations of NV centers corresponding to four edges in a tetrahedral diamond lattice. Each externally applied field such as B or σ will in general have different projection onto four different NV orientations. Therefore, an ESR spectrum of an ensemble of NV centers will have eight resonant frequencies, four ω_- and four ω_+, centered around four different ω_c's.

For simplicity, we will focus on two different NV orientations. Let us assume we can produce different temperature drift coefficients c for the two different orientations. We could then calibrate our T_{ref} in the equation 4.4 so that our two ω_c's match at the T_{ref}. If we then measure two ω_c's as the temperature changes, we will obtain $\omega_{c,i} = \omega_{ref} + c_i(T - T_{ref})$. Taking the difference between the two frequencies will give us

$$\Delta\omega_c = (c_1 - c_2)(T - T_{ref}) \tag{4.5}$$

where c_1 and c_2 depend on the NV orientation by construction. We therefore obtain an absolute temperature measurement $(T - T_{ref})$. Since our measurement precision of $\Delta\omega_c$ is finite, a larger $(c_1 - c_2)$ will amplify $(T - T_{ref})$ and create a better sensor. Because of this, we aim to experimentally create a sensor with as high $(c_1 - c_2)$ as possible.

How can we get different temperature coefficients c_i? Let us first express c_i by differentiating the equation for ω_c:

$$c_i = \hbar\frac{dD_{gs}}{dT} + \hbar d_{||}\frac{d\sigma_{z,i}}{dT} - \frac{3\mu_0^2 g^2 B_{\perp,i}^2}{2\hbar D_{gs}^2}\frac{dD_{gs}}{dT} \tag{4.6}$$

Let us analyze this equation term by term:

- **Case 1:** $B = 0$, $\sigma = 0$

  With no external fields, each NV orientation has the same c_i since $\frac{dD_{gs}}{dT}$ does not depend on NV orientation. Therefore, we cannot make an absolute temperature sensor without external fields.

- **Case 2:** $B = 0$, $\sigma \neq 0$

  While externally applied electric field and strain should not vary with temperature of the sample, we could modify dD_{gs}/dT by engineering an anisotropic external strain which confines temperature expansion in one direction. In this way, $\frac{d\sigma_{z,i}}{dT}$ would effectively be different for different orientations. The magnification factor for absolute temperature sensing would be $c_1 - c_2 = \hbar d_{||}\left(\frac{d\sigma_{z,1}}{dT} - \frac{d\sigma_{z,2}}{dT}\right)$.

- **Case 3:** $B \neq 0$, $\sigma = 0$

External magnetic field influences ω_c through its perpendicular component $B_\perp$ in the second order correction to the energy eigenvalues. Magnetic field itself does not change with temperature, but the second order energy correction depends on D_{gs} which does change with temperature, thus making $\frac{d\omega_c}{dT}$ non-zero. Therefore, the magnification factor for absolute temperature sensing would be $c_1 - c_2 = \frac{3\mu_0^2 g^2}{2\hbar D_{gs}^2}\frac{dD_{gs}}{dT}\left(B_{\perp,1}^2 - B_{\perp,2}^2\right)$.

To determine which method maximizes $c_1 - c_2$, we need to consider experimentally possible orders of magnitude for external fields. Ref. [13] explored pressure dependence of D_{gs}, and found that it varies highly linearly as $dD_{gs}/dp = 14.6$ MHz/GPa. We could exploit this dependence in the following way. Assume we clamp our diamond sample in one direction so that it cannot expand. Additionally, assume diamond has temperature expansion coefficient α_t and isothermal compressibility β. If we heat up the diamond for δT, it would want to expand for $\delta x = \alpha_t \delta T$. However, the clamp is disabling this expansion, thus exerting a pressure $\delta p = -\delta x/(\beta L)$, where L is the size of the sample's side. We can now derive that $\delta p/\delta T = -\alpha_t/(\beta L)$. Therefore, D_{gs} varies as

$$\frac{dD_{gs}}{dT} = \frac{dD_{gs}}{dp}\frac{dp}{dT} = -\frac{\alpha_t}{\beta L}\frac{dD_{gs}}{dp} \tag{4.7}$$

This variation would be orientation dependent since the pressure would be anisotropic. The challenge with this method is to apply high pressure without breaking the diamond. Another challenge is that the laser light exciting NVs in the diamond will couple out from the diamond on the sides where it touches the clamp since we will no longer have diamond-air interface, but diamond-metal, and metal is an absorber. This will reduce the number of the NVs addresses in a bulk sample and disable using the diamond as a light-trapping diamond waveguide, since the light would not be able to bounce around the diamond. Theoretically, the limiting case to changing the temperature expansion coefficient is to completely disable any expansion in one direction, while expansion in the other direction remains unchanged, $\frac{dD_{gs}}{dT} \approx -74\frac{kHz}{K}$. Therefore, the theoretical limit for $c_1 - c_2$ obtained by an external strain is 75 kHz/K.

To obtain the magnitude of the external magnetic field needed to achieve this theoretical limit imposed by strain, we need to consider orders of magnitude in the equation $c_1 - c_2 =$

$\frac{3\mu_0^2 g^2}{2\hbar D_{gs}^2}\frac{dD_{gs}}{dT}\left(B_{\perp,1}^2 - B_{\perp,2}^2\right)$. Taking into consideration the tetrahedral structure of the diamond lattice and its bond angle of 109.5°, the maximal value of the expression $\left(B_{\perp,1}^2 - B_{\perp,2}^2\right)$ is $0.94B^2$. Therefore, we would need to apply a magnetic field of 86 mT in order to achieve the theoretical limit for $c_1 - c_2$ imposed by the strain. Applying magnetic field is fairly easily doable with Helmholtz coils or a Halbach array, as it will be explain in the chapter 5. However, as we derived in chapter 2, perpendicular magnetic field mixes energy eigenlevels which causes the ESR contrast to decay. Ref. [18] measured ESR signal at different values of perpendicular magnetic field, as shown in Figure 4-1. We can see from it that at around $B_\perp = 110$ G, the contrast almost disappears.

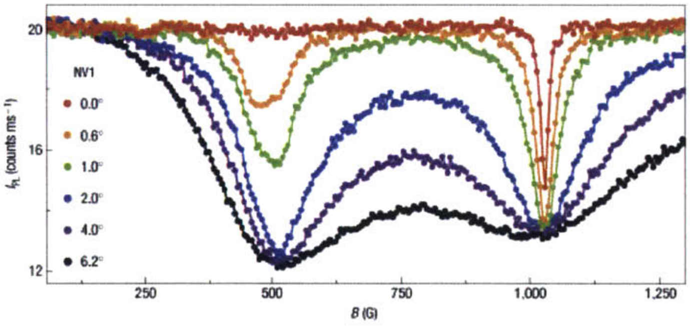

Figure 4-1: ESR contrast dependence on the perpendicular magnetic field, adapted from [18]. Instead of sweeping microwave frequency, the authors sweep magnetic field magnitudes and measure ESR for different field alignments. For $B = 1030$ G, a misalignment of 6.2°, amounting to $B_\perp = 110$ G, almost completely destroys the contrast (black line).

Whatever the way of creating $(c_1 - c_2)$ difference, our goal for absolute temperature sensing is to measure $\Delta\omega_c = (c_1 - c_2)T$. In the following sections, we propose two ways to do this - a continuous wave excitation protocol and a pulsed excitation protocol.

4.2.2 Continuous wave protocol

The temperature drift measurements done in this thesis used CW protocol. Although we measured temperature dependence for only one NV population, without inducing the difference in $(c_1 - c_2)$, the same method would apply if there was such a difference as well.

The measurement description is the same as for CW magnetometry, with the difference that we are now extracting ω_c. Ref. [10] used this method to do magnetometry and thermometry in parallel due to the fact that we can separate ω_c and $\Delta\omega$.

4.2.3 Pulsed protocol

Ref. [21, 27] used pulsed protocols for NV based thermometry. Since the goal is to measure ω_c while decoupling from the influences that shift $\Delta\omega$, the used pulse sequences were analogous to spin-echo refocusing sequence described for pulsed magnetometry. In this way, we cancel out phase shift imparted by the axial magnetic field. We now present an extension of this protocol that can be used for absolute temperature sensing. In this, we assume that the difference in c was created by the perpendicular magnetic fields, but in principle this method can be used for absolute thermometry no matter how $(c_1 - c_2)$ was created.

The largest $(c_1 - c_2)$ difference will be achieved if we aligned the external field with one of the orientations, thus making the other three orientations degenerate. If the magnitude of applied magnetic field is B, the degenerate orientations (NV1 in later text) will be exposed to $B_{||} = 0.47B$ and $B_{\perp} = 0.88B$, while the aligned orientation (NV2) will be exposed to only $B_{||} = B$. The diagram of the corresponding energy levels is shown in Figure 4-2.

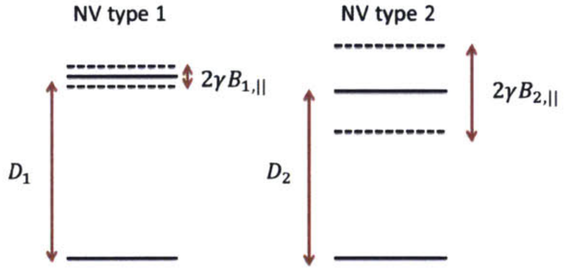

Figure 4-2: Two types of NVs based on different magnetic field projections.

Since we are modulating the dependence on temperature of zero field splitting energies, we will express them as $D_1 = D_0 + c_1 T$ and $D_2 = D_0 + c_2 T$, where D_0 is the zero field splitting at the lab temperature ($D_0 \approx 2.87$ GHz).

The goal of the pulsed protocol is to measure $c_1 - c_2$ while decoupling the system from the parallel magnetic field in order to avoid decreased sensitivity due to field fluctuations (field fluctuations will, however, reduce the sensitivity through the perpendicular component affecting c_1 and c_2). In order to do this, we propose applying a spin-echo protocol which will measure the phase difference accumulated for time τ by the two types of NV's, $\exp[-i(c_1 - c_2)T\tau]$.

The steps of the protocol go as follows (simultaneous for both NV1 and NV2):

1. prepare NVs into ground states, $\psi_0 = |0\rangle$, by green laser excitation

2. apply a $\pi/2$ pulse at the frequency D_0; this will put both types into superposition state $\psi_1 = (|0\rangle + |B\rangle)/\sqrt{2}$, where $|B\rangle = (|+\rangle + |-\rangle)/\sqrt{2}$

3. allow for free time evolution for $t = \tau$; this puts states into

$$\psi_2 = \frac{e^{-i\omega_0\tau}\,|0\rangle + \left(e^{-i(\omega_0+D+\gamma B_{||})\tau}\,|+\rangle + e^{-i(\omega_0+D-\gamma B_{||})\tau}\,|-\rangle\right)/\sqrt{2}}{\sqrt{2}}$$

4. apply a 2π pulse to swap populations between $|+\rangle$ and $|-\rangle$, putting the system into state

$$\psi_3 = \frac{e^{-i\omega_0\tau}\,|0\rangle - i\left(e^{-i(\omega_0+D+\gamma B_{||})\tau}\,|-\rangle + e^{-i(\omega_0+D-\gamma B_{||})\tau}\,|+\rangle\right)/\sqrt{2}}{\sqrt{2}}$$

5. allow for another $t = \tau$ time evolution in order to erase the phase imparted by the magnetic field:

$$\psi_4 = \frac{e^{-2i\omega_0\tau}\,|0\rangle - i\left(e^{-2i(\omega_0+D)\tau}\,|-\rangle + e^{-2i(\omega_0+D)\tau}\,|+\rangle\right)/\sqrt{2}}{\sqrt{2}}$$

6. apply a $\pi/2$ pulse to refocus the state back into $|0\rangle$

7. project the state onto $|0\rangle$ by applying green laser excitation

The signal obtained after this pulse sequence should be proportional to $S \propto (1 - \cos(2D\tau))$.

This sequence has already been used to precisely measure the zero field splitting in Ref. [21]. The additional complexity in our experiment comes from the fact that we have two NV populations with different D_i. Our signal will therefore be composed of two parts:

$$S = C(2 - \cos(2D_1\tau) - \cos(2D_2\tau)) = C'(1 - \cos(\omega_f\tau)\cos(\omega_s\tau)) \tag{4.8}$$

where C' is the normalization constant depending on our contrast, $\omega_f = (D_1 - D_2)/2 = (c_1 - c_2)T/2$ is the fast beating frequency, while $\omega_s = (D_1 + D_2)/2 = (c_1 + c_2)T/2$ is the slow envelope frequency. Therefore, by measuring ω_f we can extract the absolute temperature measurement as $(c_1 - c_2)T = 2\omega_f$.

The step 4 in the presented protocol assumes that the laser linewidth is broad enough so that it addresses frequencies detuned by $\pm g\mu_0 B_z$ from the resonance. If this is not the case, the protocol can be modified by first addressing one set of states (for example $|0\rangle$ and $|+\rangle$), then applying three consequent π pulses for $|0\rangle$ - $|+\rangle$,$|0\rangle$ - $|-\rangle$, $|0\rangle$ - $|+\rangle$. In this way the population will be swapped between $|+\rangle$ and $|-\rangle$ states. This was done in Ref. [?].

4.2.4 Sensitivity limit of a temperature sensor

For one NV measuring temperature, the theoretical sensitivity limit can be expressed as

$$\delta T = \frac{1}{dD/dT\sqrt{T_{coh}t}} \tag{4.9}$$

where T_{coh} is the relevant coherence time, t is the integration time and $dD/dT = c$ is the temperature drift coefficient we are modulating [21]. This formula does not take into account experimental imperfections such as collection efficiency and contrast. For an ensemble with N NVs, the sensitivity will scale as $\delta T/\sqrt{N}$, the standard shot noise limit.

4.2.5 Theoretical limit to sensitivity

The sensitivity limits for both magnetometry and thermometry scale as $1/\sqrt{N}$ with the N NVs. However, this is not the most strict fundamental limit for sensitivity - theoretically, we can beat the shot noise limit by using a non-classical state of a quantum system which will bring us down to the Heisenberg limit, $\delta T/N$ [25] (or $\delta B/N$). To show how this limit can be reached, we will discuss it here on the example of thermometry.

In principle, we can achieve the Heisenberg limit in sensitivity by using an entangled state of N defects. Assume we prepare our system in the maximally entangled state

$$\psi_1 = \frac{1}{2^N}\left(\prod_{N\otimes}|0\rangle + \prod_{N\otimes}|B\rangle\right)$$

If we now repeat the same pulsed protocol presented before, the accumulated phase in the $\prod_{N\otimes}|B\rangle$ state will be $\exp[-iND\tau]$, which will produce a signal proportional to $(1-\cos(ND\tau))$. With this we get a Heisenberg limited sensitivity

$$\delta T_H = \frac{1}{NdD/dT\sqrt{T_{coh}t}} = \frac{\delta T}{N} \tag{4.10}$$

We cannot obtain absolute temperature measurement in this way since our signal will be proportional to the sum of temperature drifts instead of a difference, but we can significantly improve temperature sensing without a reference as in [21]. To achieve this, we would need to be able to entangle N NV centers, with N as large as possible. So far, only $N = 2$ entanglement has been demonstrated in Ref. [16].

Chapter 5

Experimental setup and techniques

One advantage of using NVs for sensing over trapped atoms or molecules is that the NVs are naturally trapped in the solid-state diamond lattice. Because of this, NVs do not undergo Doppler broadening and can be easily localized. Moreover, the ground state ESR spectrum has sharp resonances at the room temperature, so NVs do not require cooling. For all these reasons, the sensing setups using NVs are significantly less complicated than cold atoms setups.

All the experiments reported in this thesis were performed in a laboratory setup at Research Laboratory of Electronics (RLE) at MIT. In building the setup, we were trying to minimize the size of all the setup components so that we can eventually transfer the entire setup onto a PCB. The broader idea is to make high-precision NV-based on-chip sensors for magnetic field and temperature, and to be able to integrate these chip sensors into a larger setup needing a high precision measurement. Therefore, we first present the laboratory setup, and then discuss how we could assemble these components onto a chip.

5.1 Laboratory setup

The essential parts of our setup, shown in Figure 5-1, are the NV bulk sample, an excitation laser which transfers electrons from the ground to the excited state, a microwave source which rotates electrons between the spin states of the ground state, and a fluorescence collection apparatus which collects red NV fluorescence and sends the signal for further processing. In order to test magnetic field and temperature sensing capabilities of our NV sample, we also need an external magnetic field source and temperature control. We will describe each one of these components in more detail.

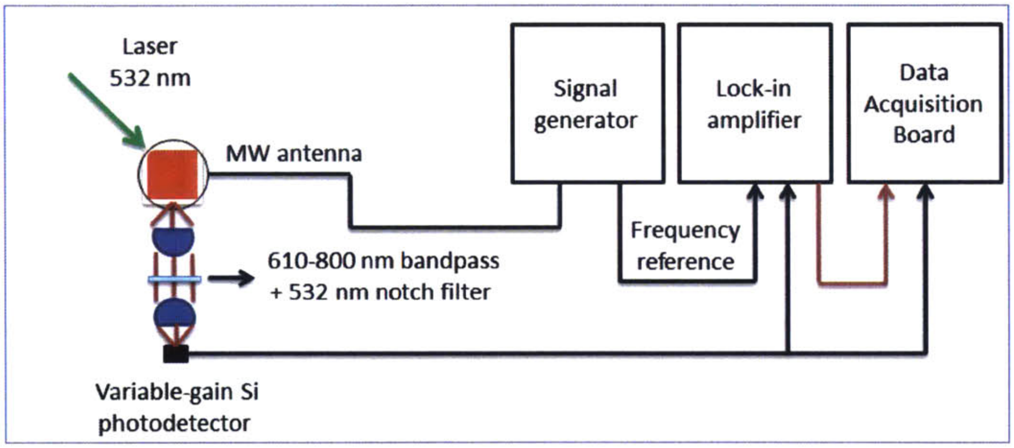

Figure 5-1: Laboratory setup for sensing. The laser is focused onto the notch of LTDW (sample shown in red). We collect fluorescence from one side of the sample and refocus it onto the photodetector with two condenser lenses. We monitor both the raw output of the photodiode and the lock-in output through a Data Acquisition Board. Lock-in amplifier uses the modulation frequency of the microwave antenna as a reference, and outputs a filtered out signal (shown in red).

In principle, we can use any laser wavelength shorter than NV's ZPL of 637 nm to excite electrons to the vibrational band above the excited state. The most convenient wavelength to use (and the one always used in NV experiments) is 532 nm green laser, due to wide availability of frequency doubled lasers. Because we are not resonantly driving the NVs, the laser does not have to be locked to a specific frequency.

A bulk diamond sample with N NVs promises a $\sqrt{N}$ increase in the magnetic field and temperature measurement sensitivity. In order to take advantage of this improvement, we need to design our sample so that we maximize N, i.e. simultaneously address as many

NVs as possible. So far, the best bulk diamond excitation scheme is to use a light-trapping diamond waveguide (LTDW) sample [10]. The LTDW we used in experiments is a type IIa diamond rectangular prism (3 x 3 x 0.3 mm) with a 45° facet on one corner (Fig. 5-2). We couple the laser through the facet and let it internally reflect many times, thus addressing a high number of NVs. With the help of the facet, laser beam couples in so that it can fulfill the total internal reflection condition in the diamond ($\theta > 24.6°$). Simulations of beam propagation show that LTDW sample allows for path lengths of over a meter [10]. Previous work shows that using the described LTDW sample, we are able to address up to $N \approx 10^{13}$ NVs.

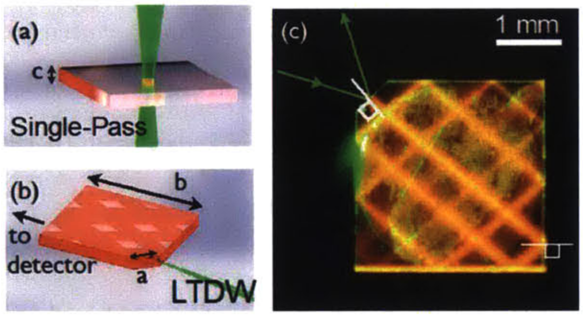

Figure 5-2: Our bulk diamond sample is a Light-Trapping Diamond Waveguide (LTDW). LTDW is more efficient than a single-pass setup (a) because it extends the beam path by several orders of magnitude through total internal reflection (b). We couple the laser in through a small notch at one end, and let the beam bounce multiple times (c). Image adapted from [10].

Bulk NV experiments commonly use single-pass geometries to excite NVs (Fig. 5-2a), but the LTDW was shown to address about two to five orders of magnitude more NVs than the single-pass setup [10]. Another advantage of LTDW is that the sample and the excitation lie in the same plane so we could confine them to a planar chip structure.

Once we excite a large number of NVs, we need to efficiently collect their fluorescence. This is an experimental challenge since most of the emitted light stays confined within the diamond slab. An excited NV can radiate in any direction; only the light rays that do not fulfill TIR condition can go out from the diamond. For the air-diamond interface, this amounts to 27% of the emission that escapes the diamond [10]. Bulk sample emits fluorescence into the full solid angle, so we need a high NA collection setup to maximize our signal. We achieve high NA by using a pair of condenser lenses facing each other (Fig. 5-1). The diverging rays fall onto the first lens and become collimated. After passing through the second lens, the rays are focused onto a point, which we align with the Si photodiode chip. Between the lenses, we put a bandpass filter (610 – 800 nm) to filter out NV^0 fluorescence and possible IR laser line (our laser is a frequency doubling laser which begins with 1064 nm, so there can still be some remaining IR component). We also add a laser line notch filter (filters out green fluorescence) to avoid collecting the excitation light. The variable gain Si photodiode at the end of the imaging setup converts fluorescence to voltage, which we input into a Data Acquisition Board connected to the computer. This signal gives us a raw ESR spectrum. One part of the photodiode voltage signal also goes to the lock-in amplifier which gives a processed signal we further use for sensing.

We rotate electrons among different spin states of the ground state with a microwave excitation equal to the zero field splitting of ≈ 2.87 GHz (we get multiple resonant microwave frequencies due to Zeeman splitting when we apply the external magnetic field). The microwave field is delivered by a microwave antenna positioned above our planar sample. The antenna's oscillation frequency is set by a signal generator, which we adjust to provide a frequency sweep around the resonant frequencies. Additionally, we frequency modulate the microwave signal at 1000 Hz, and output the modulation frequency as a reference signal to the lock-in amplifier. We use the lock-in amplifier to filter out the laser noise and other low-frequency noise sources. Furthermore, we filter out fluorescence from the NVs that are excited with a laser, but are not driven with the microwave source. The lock-in amplifier filters out a signal at a particular frequency; in this case we filter out a signal which is modulated at the modulation frequency of the microwave antenna. The lock-in output is input into the Data Acquisition Board - this is our ESR signal used for sensing. The comparison of a raw ESR signal (straight from the photodiode) and the lock-in output is shown in Figure

5-3. We extrapolate resonant frequencies from the lock-in signal by looking at its crossings of the x-axis. The lock-in signal is the first derivative of the raw signal.

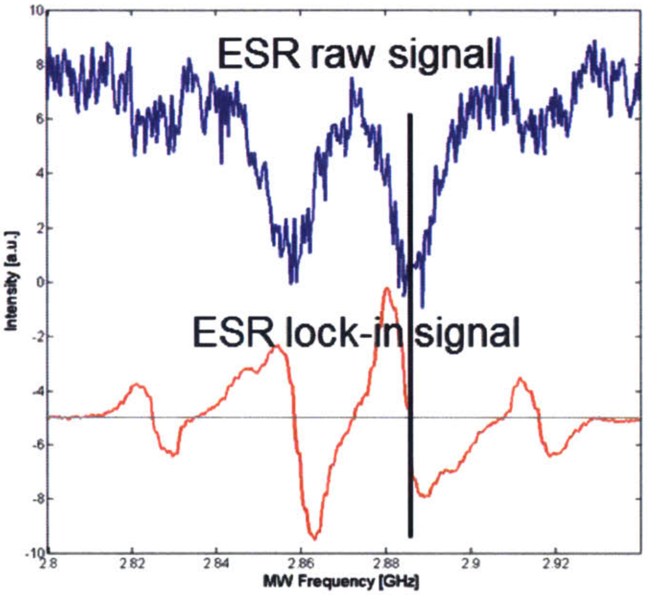

Figure 5-3: Comparison of the raw ESR signal and the lock-in output. The lock-in amplifier filters out all frequencies other than the modulation frequency. We can match each resonant dip of the raw ESR signal to a zero-crossing of the lock-in signal. For sensing experiments, we monitor the shifts of the resonant frequencies.

Finally, in order to test sensing capabilities of our setup, we need to be able to control the external magnetic field and sample temperature. We control the sample temperature with thermoelectric coolers (TECs, Peltier coolers) mounted on the sample holder. We made our sample holder out of copper in order to have a good thermal conductivity. Copper and diamond are among the best thermal conductors in nature (thermal conductivity: copper 401 W/mK, diamond 1000 W/mK; for comparison brass 109 W/mK, water 0.58 W/mK [3]). We can therefore assume that our sample equilibrates with TECs almost instantaneously.

We apply external magnetic field with a Halbach array (Fig. 5-4). Halbach array is a plastic ring with permanent magnets positioned around the rim. Permanent magnets are positioned in such as way that they make a uniform magnetic field inside the ring. The

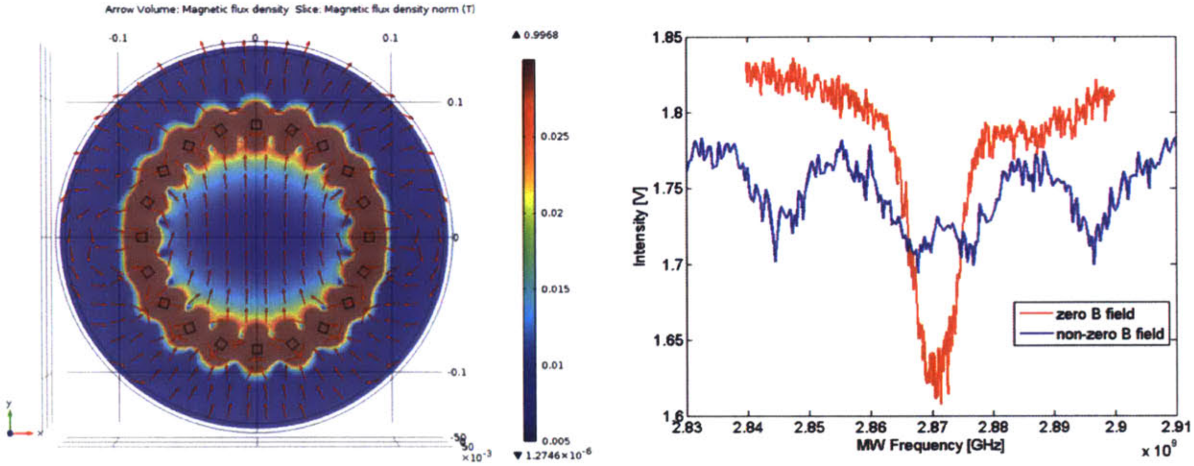

Figure 5-4: (Left) Simulation of magnetic flux density in a Halbach array. Arrows show the direction of the magnetic field. We can see that the field inside the ring is uniform and in the plane of the ring. (Right) Comparison of raw ESR with and without external magnetic field for the same NV orientation. The magnetic field splits spin $|1\rangle$ state into $|\pm 1\rangle$ states, which are further split into hyperfine levels. The split levels are centered around the zero field splitting.

field direction is in the plane of the ring. We put the ring around our sample so that the sample is in its center (where the field is most uniform.) We can rotate the ring to change the field direction. Our Halbach array provides $B \approx 60$ G. The advantage of Halbach array over Helmholtz coils is that permanent magnets are less noisy; Helmholtz coils suffer from the noise from the current source (especially when the currents are high). The drawback of Halbach array is that we have less freedom in controlling the magnetic field direction.

We test the Halbach array and calibrate its orientation by looking at the raw ESR signal. Figure 5-4 shows the comparison between the zero field and non-zero field ESR. When we turn on the magnetic field, we get multiple resonance frequencies centered around the zero field splitting. We can rotate Halbach array until we achieve the desired field position. We most frequently use one of the two positions - all four orientations split differently (eight overall resonances) or three degenerate orientations plus one non-degenerate (four overall resonances).

5.2 On-chip diamond sensor

An on-chip diamond sensor should contain an excitation laser, bulk diamond, fluorescence collection apparatus, a photodiode, and an antenna. Antenna input and photodiode output would be connected with BEC cables with the rest of the setup.

For laser excitation we can use a compact laser diode. Moreover, we could couple laser diode to an optical fiber, and then align the fiber end next to our sample prism facet. Our LTDW sample is planar (3 x 3 x 0.3 mm) and chip compatible. We can use unmounted photodiodes for fluorescence detection. Planar antennas can be made by using Printed Circuit Boards (PCBs). We could then put the sample directly on top of a PCB antenna (designing a PCB antenna that produces the most uniform microwave excitation is another engineering challenge). The remaining challenge is to make the fluorescence collection apparatus more compact.

When it comes to on-chip sensing, the main focus of this thesis was designing the on-chip collection apparatus. We propose to use a combination of a ball lens and a half-ball lens placed next to LTDW, and to place a filter glass waveguide at the focus of the lens. The other edge of the waveguide would be directly connected to the photodiode. Here we present the calculations for the collection efficiency of the ball lens, as well as ray tracing results from which we can determine the optimal waveguide position.

5.2.1 Collection efficiency

Our objective is to collect as much fluorescence as possible from a 3 x 3 x 0.3 mm sample. Since the sample radiates in all directions, we cannot image it. The best we can do is to collect and focus as much fluorescence as possible onto the photodetector, even if the light rays come at arbitrary angles. This will certainly reduce our detection efficiency since according to Fresnel equations the reflectance of the photodiode increases as the incidence angles increaase. The first step, however, is to turn highly diverging light rays emitted by the sample into converging or collimated rays. Since we need a high NA collection device, we propose using a ball lens of high refraction index. As a reference refraction index we use

$n = 2$ since that is the index of S-LAH79 material, used in commercial ball lenses [2].

We will first calculate which fraction of light we can collect with a ball lens placed next to our sample. Then we will do ray tracing simulations to depict how the rays collected by the ball lens behave, and where we can put the photodiode. Another challenge with an on-chip detection is that we cannot put the photodiode too close to the microwave antenna since it will pick up its signal. Therefore we need to add a waveguide between the sample and the photodiode. For the waveguide we propose using a long-pass filter glass rectangular slab which we made by cutting a filter glass and polishing its edges.

We take into consideration two ways of placing the sample with respect to the lens - one shown in Figure 5-5 and the other rotated for 45°. In the case of the first position, we collect the light from three sides - one face side and two edges. In the tilted sample case, we collect light from two sides, but same amount from both.

Collection efficiency, e, is defined as the ratio of the solid angle Ω_c captured by the lens to the total irradiated solid angle, which is in our case 2π from each side of the rectangular box of the sample. The solid angle is in general calculated as

$$d\Omega_c = sin(\theta) d\theta d\phi \tag{5.1}$$

where θ and ϕ are spherical coordinates in the x-y and z planes, respectively. In order to compare the collection efficiency of a spherical lens combined with two different positions of the sample, we will calculate the collection efficiencies from each side of the sample, but not from the top of the sample since the collection from the top is the same no matter how we rotate the sample.

For the sample positioned straight (Fig. 5-5), the relevant sides from which the light is collected are the face side (θ_1 angle in Figure 5-5) and the edge sides (θ_s in Figure 5-5). The marginal rays which determine θ_1 and θ_s are perpendicular to the lens sphere, and therefore perpendicular to its radius. From the geometry of the sample we can see that the angle ϕ is equal to θ_1, and same for both the edge and the face sides. For the tilted sample shown in Fig. 5-6, two sides contribute to the collection efficiency. The marginal ray θ_s is shown in

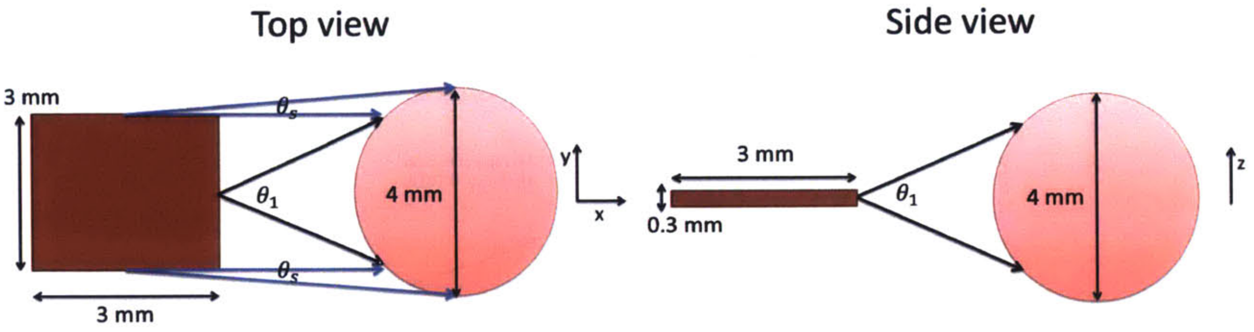

Figure 5-5: Relevant angles for the calculation of the collection efficiency of light irradiated from the sample by a ball lens. (Left) Top view of the sample and (right) side view.

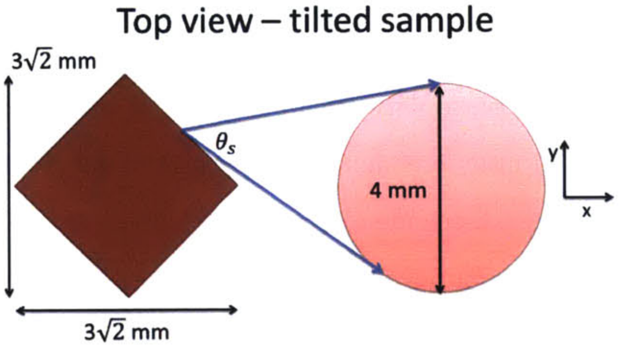

Figure 5-6: The top view of the tilted sample with the relevant angle. The side view is the same as for the straight sample, but the effective side width is a $\sqrt{2}$ times longer.

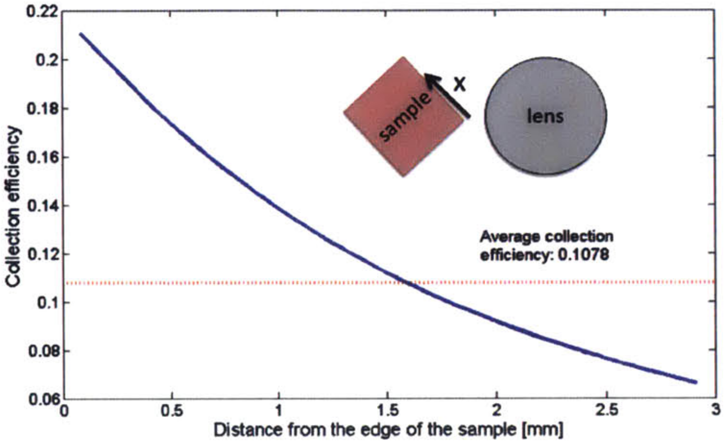

Figure 5-7: Dependence of collection efficiency for the tilted sample versus the distance from the point on the sample closest to the lens.

Fig. 5-6, while ϕ is the same as for the straight sample.

We numerically find θ_s angles, whereas θ_1 angle can be easily analitically found. Since the goal of this calculation is to determine a more optimal sample position (the collection efficiency will monotonically increase with the decrease of distance between the lens and the sample), we use a reference sample-lens distance of 2 mm. We calculate collection efficiency from every point on the sample's face side and edges. The results are shown in Figures 5-7,5-8 and 5-9. Since each point contributes equally to the overall efficiency, we can just take the mean efficiency as our figure of merit. After adding up the efficiencies from the relevant sides, we get that the tilted sample has the overal collection efficiency $e_t = 2 \times 0.1078/4 = 0.0539$, whereas the face sample has $e_f = (0.1869 + 2 \times 0.0016)/4 = 0.0475$. We therefore conclude that the tilted position is preferable. However, the difference in collection is not dramatic (0.64% more collection for the tilted sample) while the tilted sample position may introduce further difficulties such as laser scattering from the corner of the sample.

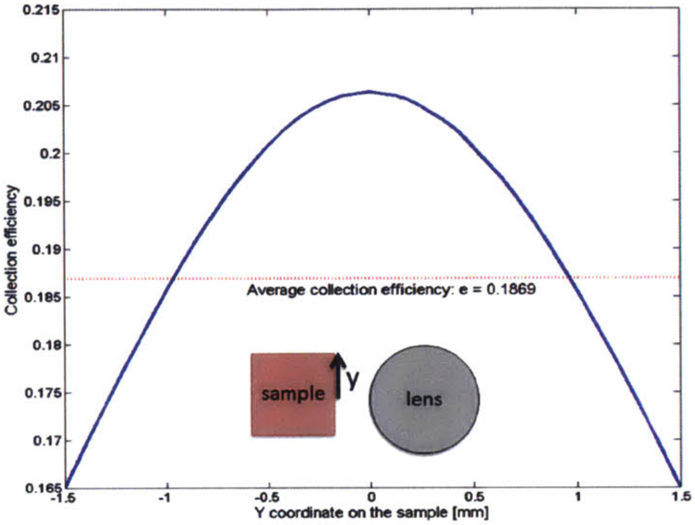

Figure 5-8: Dependence of collection efficiency for the face sample versus the distance from the center of the sample.

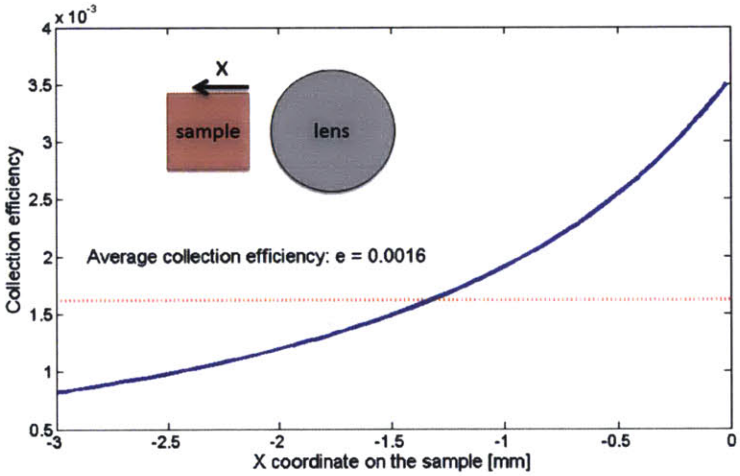

Figure 5-9: Dependence of collection efficiency for the face sample's edge versus the distance from the point on the sample closest to the lens.

5.2.2 Ray-tracing simulations

Now that we concluded what is the optimal position of the sample in front of a ball lens, we want to explore how the light rays behave once they go through the ball lens. We do this through ray tracing simulations, done by the OpticalRayTracer open source software.

Figure 5-10 shows a simulation of the behavior of a ball lens with $n = 2$ and radius $r = 2$ mm (one square in the simulation corresponds to 1 × 1 mm). We see that putting the waveguide around 4 mm away from the ball lens would be the most optimal position. However, we would like to see if it is possible to reduce the NA of the converging light rays. We can reduce the NA (and therefore couple more light rays into the waveguide) if we put another half-ball lens in the focus of the ball lens (simulation shown in Figure 5-11).

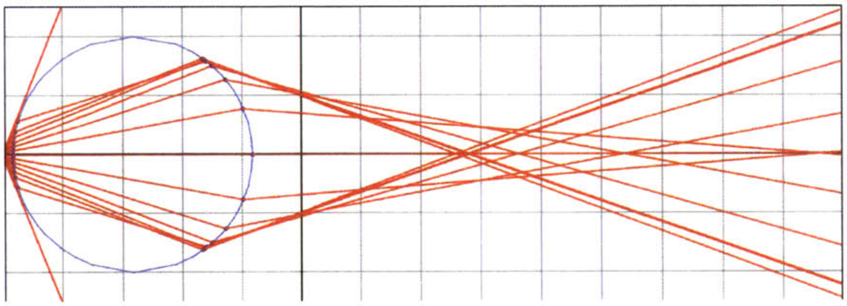

Figure 5-10: Ray tracing simulation for a ball lens ($n = 2$) placed in front of a diverging source on the optical axis.

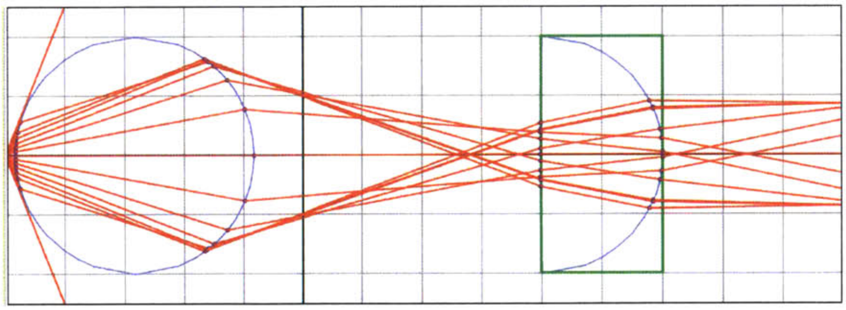

Figure 5-11: Ray tracing simulation for a ball lens and a half-ball lens ($n = 2$) placed in front of a diverging source on the optical axis.

Figures 5-11 and 5-10 show the behavior of rays from a diverging source on the optical axis. Since our sample is macroscopic, we need to see how the diverging rays offset from the optical axis behave as well. A simulation of a ball lens with an offset source is shown in Figure 5-12. The simulation shows that an offset in the source produces an offset in the focus. Therefore, our waveguide needs to be at least as wide as the sample itself.

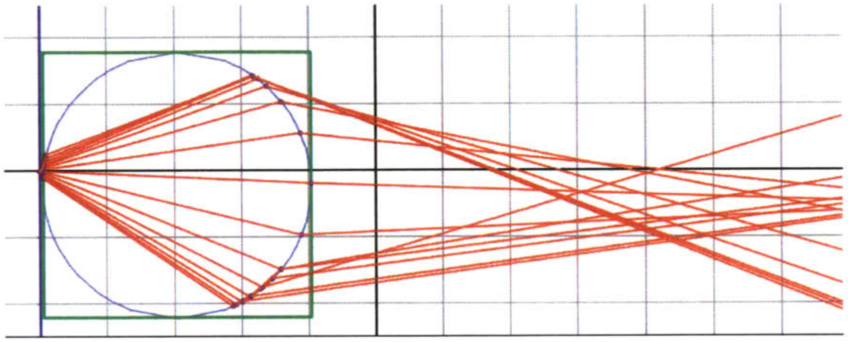

Figure 5-12: Ray tracing simulation for a ball lens ($n = 2$) placed in front of a diverging source offset from the optical axis.

In the laboratory setup we use two condenser lenses to focus the fluorescence onto the photodetector. Condenser lenses collimate the rays between them, so we can in principle put them at an arbitrary distance and preserve the same collection (that is how we avoid interference of the antenna signal with the photodiode in the lab setup). The problem with using condenser lenses for the on-chip setup is that they behave as condenser lenses only if the sample is approximately a point source with respect to the lens' size. For the lab setup we use condenser lenses of a around 2.5 cm in radius. If we would use the same setup on-chip, we would lose the planar structure altogether. Some of the smallest condenser lenses on the market have diameters of $7 - 10$ mm [2, 4]. One can find small half-ball lenses which behave as condenser lenses if we obey the required spacing between them (for a 2 mm radius half-ball lenses, spacing should be around 0.7 mm - Fig. 5-13). The simulation of two half-ball lenses at an optimal distance is shown in Figure 5-13, while the simulation two half-ball lenses at an arbitrary distance is shown in Figure 5-14. We can see that this system changes diverging rays into converging, but with very high NA. If we use this setup for on-chip sensing, we would have to place the photodiode less than 5 mm away from the sample and the antenna, and the photodiode would most likely pick up some microwave signal. We cannot collect the light with a waveguide due to a very high NA. Therefore, we are left with either using two large condenser lenses and giving up on the planar structure, or with using a ball lens, a half-ball lens and a waveguide.

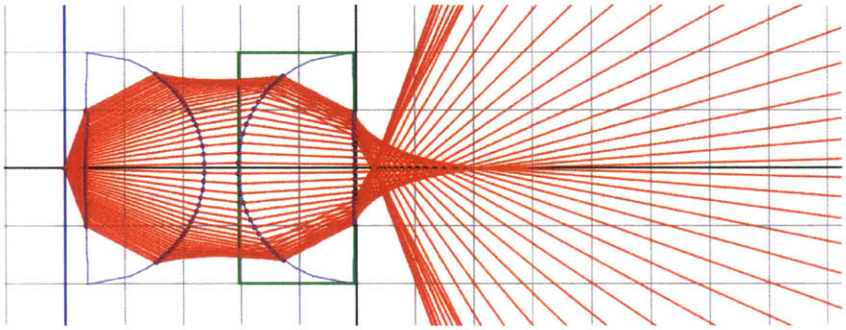

Figure 5-13: Ray tracing simulation for two half-ball lenses ($n = 2$) placed in front of a diverging source on the optical axis. Simulation reveals that the rays between the lenses are not collimated, so there is an optimal distance between the lenses for achieving the focus equal to around 0.7 mm for 2 mm radius lenses.

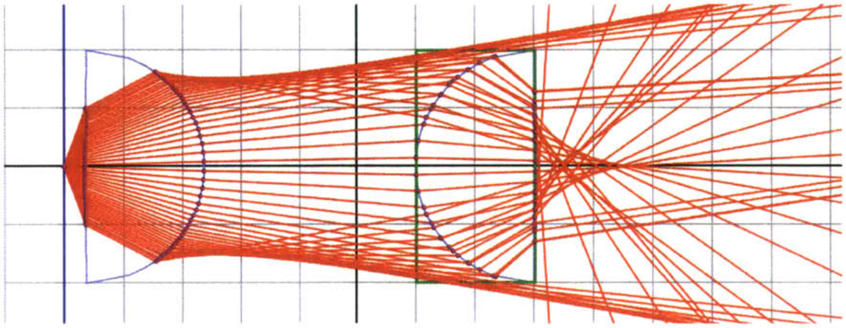

Figure 5-14: Ray tracing simulation for two half-ball lenses ($n = 2$) placed in front of a diverging source on the optical axis at an arbitrary distance.

5.2.3 Discussion of the results

Our collection efficiency calculations and ray tracing simulations reveal a couple of trade-offs one needs to make when designing on-chip collection setups.

- **Sample position:** Collection efficiency calculations show that a sample tilted at 45° produces a better collection efficiency when coupled to a ball lens then a straight sample. However, ray tracing simulations show that a diverging sources offset from the optical axis focus at offset points after the ball lens. Since the tilted sample has $\sqrt{2}$ times larger size in the $x-y$ plane than a straight one, the focus of rays after the ball lens would also be more smeared and we would need a wider waveguide and a wider photodetector to achieve the same collection.

- **Choice of lenses:** Ray tracing simulations show that a ball lens combined with a half-ball lens produces more collimated rays than a single ball lens. Therefore, one of the potential designs is to use a ball lens, half-ball lens and a waveguide to couple the light into the photodetector. We can avoid the use of a waveguide if we use two large condenser lenses enough separated to isolate the microwave antenna from the photodiode, and to have our sample behave as a point source. However, in this case we would have to give up on a planar geometry of our sensor since the condenser lenses would be a couple of centimeters in diameter.

THIS PAGE INTENTIONALLY LEFT BLANK

Chapter 6

Results

As previously explained, we use ESR spectra to read off both magnetic field and temperature measurements. In general, we can distinguish two types of perturbations at the same time - those that shift the central frequency of an ESR spectrum such as temperature, perpendicular magnetic field and parallel strain/electric field, and those that separate $|\pm 1\rangle$ spin states such as parallel magnetic field and perpendicular strain/electric field. In both cases, we use lock-in output of the ESR signal. In Figure 6-1 we see an example of a lock-in output of one half of the ESR spectrum ($\omega < 2.87$ GHz). We see four resonances corresponding to four NV orientations in the diamond lattice (each orientation has a different projection of magnetic field which separates it to a different frequency). Each orientations is further split into three resonances due to hyperfine coupling. We extrapolate $\omega_c = (\omega_+ + \omega_-)/2$ and $\Delta\omega = \omega_+ - \omega_-$ by measuring intersections of the ESR signal with the x-axis on both sides of the central frequency, thus obtaining ω_+ and ω_-. Figure 6-2 shows the entire ESR signal with both ω_+, ω_- and ω_c determined.

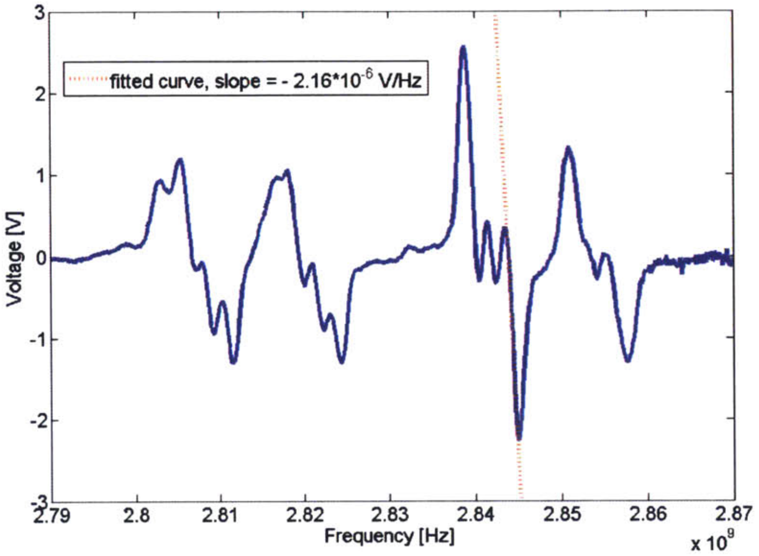

Figure 6-1: Lock-in output for $\omega < 2.87$ GHz. For sensing, we choose the sharpest transition and linearly fit its ESR slope. We use this fit value as a conversion factor between Voltage and Frequency in further calculations.

6.1 Magnetometry

We extrapolate ω_+ and ω_- by linearly fitting the lock-in slope and finding its intersection with the x-axis, as shown in Figures 6-1 and 6-2. In the presented case, the intersection frequencies were found to be $\omega_- = 2.844$ GHz and $\omega_+ = 2.903$ GHz, thus giving $\Delta\omega/2 = 0.0292$ GHz and $\omega_c = 2.8735$ GHz. Using that $g\mu_0/h = 27.9$ GHz/T since $g = 2$ for the electrons in NVs [10], we can now calculate the magnetic field projection to be $B_z = 10.6$ G.

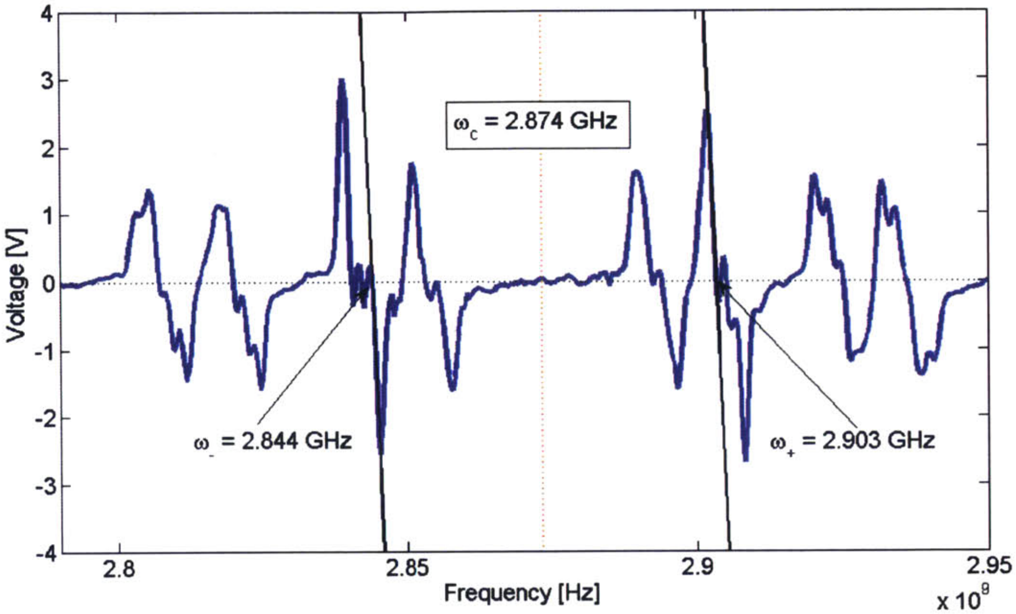

Figure 6-2: Full ESR spectrum with relevant frequencies. We determine ω_c and $\Delta\omega$ from $\omega_\pm$.

The precision of the presented measurement heavily depends on the measurement resolution. In Figure 6-1 we swept frequency between $2.79 - 2.87$ GHz in 400 steps, thus having a resolution of 200 kHz/step. The resolution-limited precision for this measurement would be 7.168μT. Since our lock-in amplifier uses a time constant of 20 ms, the equivalent noise bandwidth of detection is 12.5 Hz [1]. Therefore, the resolution-limited precision is $2\mu\mathrm{T/Hz}^{1/2}$. However, we can in principle arbitrarily reduce our resolution by taking more data points and improve our sensitivity. The question arises: what is the fundamental limit to our precision then? Theoretically, the fundamental limit is given by equation 4.3. If we plug in the values $N = 10^{13}$, $T_2^* = 1\mu$s, $\tau = 20$ ms, we get $\delta B = 1.3 \times 10^{-14}$ T or 13 fT, corresponding to 3.64 $\mathrm{fT/Hz}^{1/2}$. Here, however, we are not accounting for experimental imperfections such as limited collection efficiency and imperfect contrast. In order to estimate experiment-limited noise floor, we need to find out how stable the intersection point of the ESR and zero axis is. To do this, we first determine our intersection frequency ω_- as previously described. Then we adjust the signal generator so that the antenna drives our NVs at a constant frequency of ω_-. We take a time series voltage output of the lock-in amplifier - our DAQ is able to take up to 100 seconds of data at 1000 Hz sampling rate. We then perform frequency analysis on our data to get the noise spectrum. The voltage noise is translated into frequency noise by dividing the voltage with the measured lock-in slope (for Fig. 6-1 this is 2.16×10^{-6} V/Hz). Frequency is translated into magnetic field noise by dividing once again with 27.9 Hz/nT. Finally, with the division by the square root of the equivalent noise bandwidth, we obtain the noise frequency spectrum shown in Figure 6-3. We see that our experimental noise floor is on the order of 1 nT/Hz$^{1/2}$ in the noise frequency range between $0.01 - 10$ Hz. In particular, we can extrapolate that the noise floor at 0.1 Hz is 776.5 pT/Hz$^{1/2}$. We can improve the experimental noise floor by introducing several experimental improvements such as increasing the collection efficiency and improving the filtering of the NV fluorescence (both on the level of the lock-in amplifier and by using better optical filters). Furthermore, the noise floor goes down if the lock-in slope calculated from Figure 6-1 increases. The slope is determined by the ESR linewidth, and linewidth can be optimized in several ways, as discussed in chapter 3. Table 6.1 summarizes the obtained noise floors for magnetometry and recommendations on how they could be improved.

Source of limitation	**Noise floor [/Hz$^{1/2}$]**	**How to improve**
resolution	2μT	take more data points
experimental	1 nT	improve the setup
theoretical	4 fT	use entangled NVs

Table 6.1: Noise floor limitations for magnetometry with a given ensemble of fixed N of NVs, fixed coherence time T_2^* and fixed equivalent noise bandwidth. These parameters can be improved as well, and noise floor will go down if we increase N, increase T_2^* and decrease the lock-in time constant.

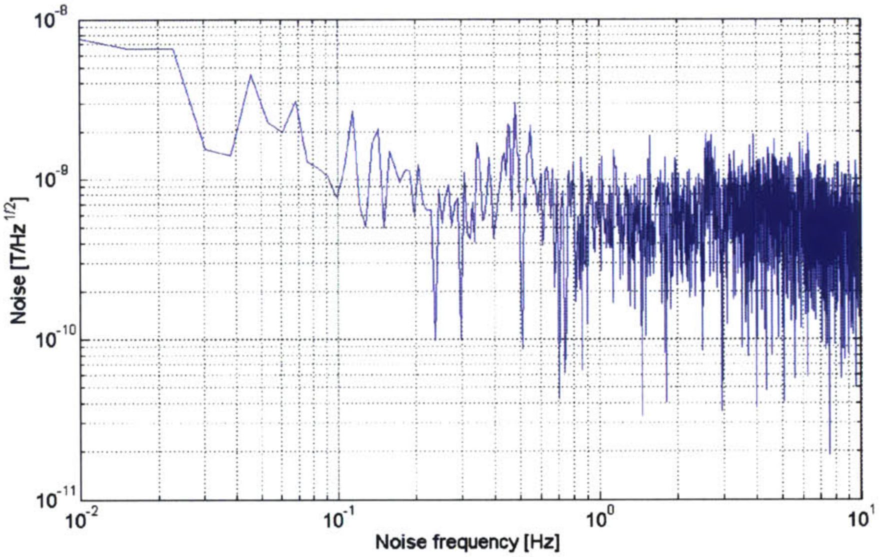

Figure 6-3: Experimental noise floor for magnetic field sensing. For example, we can read off that the noise floor at 0.1 Hz is 776.5 pT/Hz$^{1/2}$.

6.2 Thermometry

We now want to examine temperature dependence of the ESR signal. The perpendicular magnetic field we apply here is negligible (in the second order) so we also approximate that ω_c drifts only due to temperature drifts. We focus on the resonance fitted in Figure 6-1, but now we change the sample temperature using TEC coolers. After setting a target temperature, we wait for more than a minute for the sample temperature to reach equilibrium. The amplitude of microwave antenna is set to -20 dBm so that the microwaves do not interfere with TEC operation (we observed that for stronger microwave fields, TECs start giving unrealiable temperature measurements). The ESR spectra for different temperatures are shown in Figure 6-4. We see that the ESR retains its shape as we change the temperature, and all the points visibly drift.

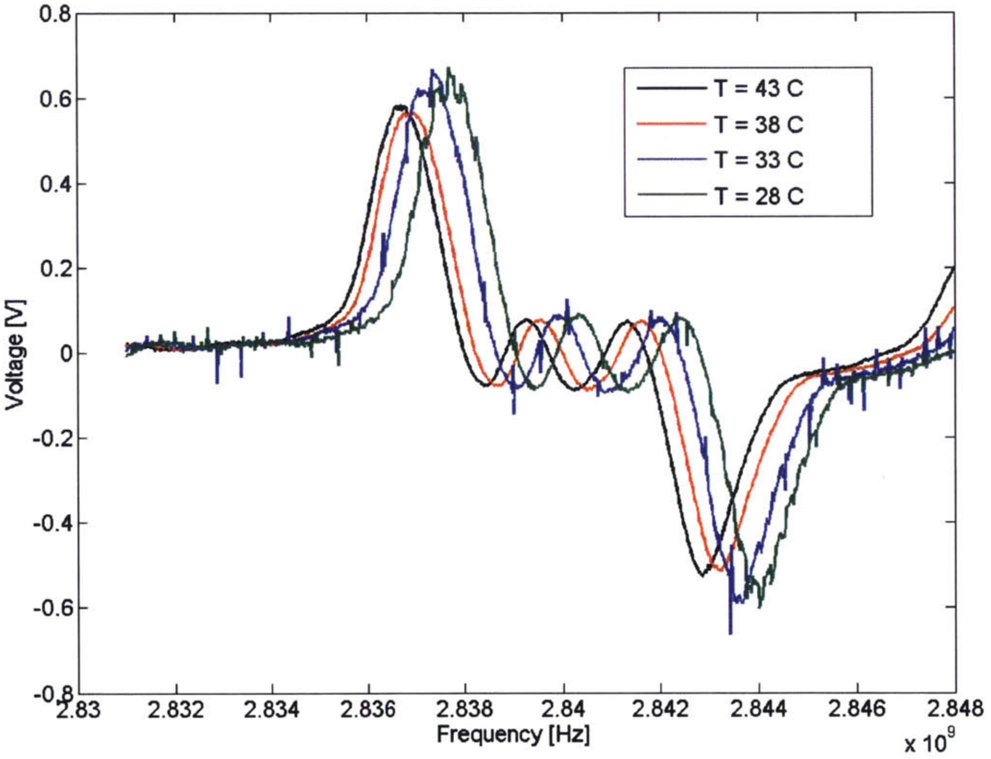

Figure 6-4: Temperature dependence of the ESR signal. The entire ESR signal shifts to lower frequencies with the increase in temperature.

We can now try to estimate the temperature drift coefficient, reported to be $-74.2\,\mathrm{kHz/K}$ [6]. We calculate shifts of the ESR signals for $T \in [33, 38, 43]$ C with respect to the signal for $T = 28$ C. The minimal shift we can resolve is given by the frequency range, 17 MHz, divided by the number of data points, 1000 - $\Delta\omega_{min} = 2\pi \times 17$ kHz. We measure the temperature shift in the number of $\Delta\omega_{min}$ units which minimize the square of the difference between the two signals. This is done in a short MATLAB script attached in the appendix. The measurement uncertainty is equal to $\Delta\omega_{min}$ while we ignore the uncertainty in temperature since it is less than 1 percent. The linear fit to the frequency shifts versus temperature differences graph is shown in Figure 6-5 (we show the absolute value of the temperature drifts, that is why the slope is positive). The obtained result is $dD/dT = -85 \pm 26$ kHz/K. The uncertainty range is quite high due to a low number of data points for the fit, but the reported value is within the measured limits.

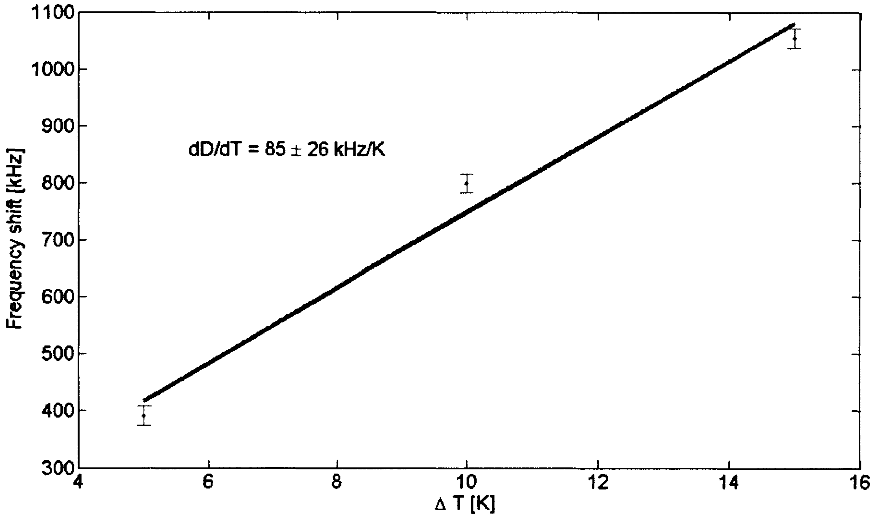

Figure 6-5: Estimation of dD/dT for the used NV sample. The estimated range of -85 ± 26 kHz/K contains the previously reported value of -74 kHz/K [6].

The sensitivity for temperature measurement is based on the same parameters as the magnetic field sensitivity, and the noise spectrum looks the same since for CW protocols we still measure temperature shifts with the precision of measuring the zero crossing of the lock-in signal. The only difference is that in the case of temperature, we convert frequency drifts to temperature drifts using the conversion factor dD/dT. With this modification, we obtain the results presented in Table 6.2. The noise improvement methods are the same as for magnetometry.

A lot of NV-based thermometry research is aimed at biosensing, for which we would

Source of limitation	**Noise floor [/Hz$^{1/2}$]**
resolution	64 mK
experimental	0.3 mK
theoretical	8.5 nK

Table 6.2: Noise floor limitations for thermometry with a given ensemble of fixed N of NVs, fixed coherence time T_2^* and fixed equivalent noise bandwidth.

possibly need to inject an NV sample into a living cell, such as in Ref. [21]. Since our sample is macroscopic, it cannot be injected without damaging the cell. Therefore, the applications of bulk NV thermometry are more suitable for external sensing, or on-chip high-precision thermometry. The sensitivities achieved in Ref. [21, ?, 27] are in the range of $5 - 10$ mK/Hz$^{1/2}$. Our setup exhibits an order of magnitude better sensitivity but at the cost of lower spatial resolution.

Chapter 7

Conclusion

The goal of this thesis was to provide a framework for making a better bulk diamond temperature and magnetic field sensor. Since we are using CW ESR spectra for sensing, this thesis explores in detail various properties of ESR. We first derive the energy level structure of an NV, including the influences of magnetic field, electric/strain field and temperature. We also model NV dynamics under CW irradiation with a laser, microwave field and infrared field. Our results suggest that an optimal ESR linewidth and contrast are achieved for low laser power and microwave power at the beginning of saturation. Microwave power improves the contrast up to saturation, but also broadens the linewidth. Our NV modeling recovers these results previously empirically obtained in Ref. [17]. While the model for results in Ref. [17] was partly phenomenological (e.g. the optical pumping was introduced phenomenologically), we derived our results using a master equation, taking into consideration dynamics of each of the relevant energy levels. Moreover, for the first time in literature we consider the influence of the infrared driving field, and find that it improves the contrast at the expense of linewidth broadening. However, an additional driving field would make the setup more complex while the contrast improvement is not very significant, so it is arguable whether we want to employ this method.

The thesis then describes sensing protocols used for magnetometry and thermometry, and derives theoretical sensitivity limits. The thesis goes one step further than the existing literature in that it proposes drift-free temperature sensing protocols built upon the previous sensing work. We also discuss pros and cons of different ways in which we could change dD_{gs}/dT, which is necessary for absolute thermometry.

The design of the sensing setup is described in chapter 5. We explain in detail the choice of different components. One of the biggest advantages of NV based sensing is that the procedure and setup can be made very simple - sensing is done at room temperature, only a few setup components are needed, and moreover all of the setup components can be miniaturized. We explore this idea in more detail by suggesting an on-chip sensor setup, and in particular, by focusing on optimizing the fluorescence collection apparatus. For the collection apparatus, we propose using a ball and a half-ball lens followed by a waveguide. If the on-chip setup would prove successful, NVs could become a commercial success, and a prime example of applied quantum physics which could drive progress both in industrial and fundamental research.

Finally, we test the sensing setup using CW magnetometry and thermometry. Our experimentally determined noise floors are on the order of 1 $\mathrm{nT/Hz^{1/2}}$ for magnetic field sensing, and 0.3 $\mathrm{mK/Hz^{1/2}}$ for temperature sensing. We discuss how we could improve our noise floors with the existing setup, as well as how the sensitivity can be improved. Some of the improvements can be fairly straightforward such as optimizing the laser and microwave powers. Other improvements, such as using entangled NVs, are less trivial, but should in any case be considered since the technological progress in quantum computing may result in a progress in quantum sensing. Bulk NVs are by all means not the most optimal systems for every sensing application, and we discuss the advantages that other systems, such as atomic vapor cells or NV nanodiamonds, may have over our setup. An important advantage of a bulk diamond sensor over vapor cells is that it is an all solid-state device, which may open its path towards a high-precision space-based sensing. Overall, we hope to have shed some new light on the fascinating area of quantum sensing, and to have motivated future research in bulk NV based sensing systems.

Appendix: MATLAB code for finding temperature shifts

```
function [ temperatureShift ] = findHorizontalShift(v1,v2,x1,x2)
% finds a horizontal shift between vectors v1 and v2 by
% minimizing the square difference on the region [x1,x2]
% the shift is expressed in the units of our experimental resolution
sums = zeros(1,(x2-x2+1));
domain_length = x2-x1+1;
shift = zeros(1,domain_length);
for i=1:domain_length+1
    shift(i)=i-1;
    shiftedVec = shiftVec(v1,i-1);
    sums(i)=sum((v2(x1:x2)-shVec(x1:x2)).^2);
end
[minVal, position] = min(sums);
temperatureShift = shift(position);
end

function [ shifted ] = shiftVec( vec,t )
% shifts a vector to the right for the amount t, adds zeros to the left
len = size(vec);
```

```
L = len(2);
shifted = [zeros(1,t),vec(1:L-t)];
end
```

Bibliography

[1] About lock-in amplifiers. Stanford Research Systems.

[2] Edmund optics. Official website, accessed on: 2015-04-20.

[3] The engineering toolbox. Official website, accessed on: 2015-04-20.

[4] Thorlabs. Official website, accessed on: 2015-04-20.

[5] V. M. Acosta, E. Bauch, A. Jarmola, L. J. Zipp, M. P. Ledbetter, and D. Budker. Broadband magnetometry by infrared-absorption detection of nitrogen-vacancy ensembles in diamond. *APL*, 97(174104), 2010.

[6] V. M. Acosta, E. Bauch, M. P. Ledbetter, A. Waxman, L.-S. Bouchard, and D. Budker. Temperature dependence of the nitrogen-vacancy magnetic resonance in diamond. *Phys. Rev. Lett.*, 104(070801), February 2011.

[7] C. D. Aiello, M. Hirose, and P. Cappellaro. Composite-pulse magnetometry with a solid-state quantum sensor. *Nat.Comm.*, January 2013.

[8] A. Alkauskas, B. Buckley, D. Awschalom, and C. Van de Walle. First-principles theory of the luminescence lineshape for the triplet transition in diamond nv centres. *New J. Phys.*, 16(073026), July 2014.

[9] D. Budker and M. Romalis. Optical magnetometry. *Nat. Phys.*, 3, April 2007.

[10] H. Clevenson, M. E. Trusheim, C. Teale, T. Schroder, D. Braje, and D. Englund. Broadband magnetometry and temperature sensing with a light-trapping diamond waveguide. *Nat. Phys.*, April 2015.

[11] A. Cooper, E. Magesan, H. N. Yum, and P. Cappellaro. Time-resolved magnetic sensing with electronic spins in diamond. *Nat.Comm.*, January 2014.

[12] M. W. Doherty, N. B. Manson, P. Delaney, F. Jelezko, J. Wrachtrup, and L. Hollenberg. The nitrogen-vacancy colour centre in diamond. *arXiv:1302.3288*, 2013.

[13] M. W. Doherty, V. V. Struzhkin, D. A. Simpson, L. P. McGuinness, Y. Meng, A. Stacey, T. J. Karle, R. J. Hemley, N. B. Manson, L. Hollenberg, and S. Prawer. Electronic properties and metrology applications of the diamond nv center under pressure. *PRL*, 112(047601), January 2014.

[14] M.W. Doherty, F. Dolde, H. Fedder, F. Jelezko, J. Wrachtrup, N.B. Manson, and L.C.L. Hollenberg. Theory of the ground state spin of the nv center in diamond: I. fine structure,hyperfine structure, and interactions with electric, magnetic and strain fields. *arXiv:1107.3868v1*, July 2011.

[15] F. Dolde, H. Fedder, M. W. Doherty, T. Nobauer, F. Rempp, G. Balasubramanian, T. Wolf, F. Reinhard, L. Hollenberg, F. Jelezko, and J. Wrachtrup. Electric-field sensing using single diamond spins. *Nat. Phys.*, 7:459, 2011.

[16] F. Dolde, I. Jakobi, B. Naydenov, N. Zhao, S. Pezzagna, C. Trautmann, J. Meijer, P. Neumann, F. Jelezko, and J. Wrachtrup. Room-temperature entanglement between single defect spins in diamond. *Nat.Phys.*, 9, 2013.

[17] A. Dreau, M. Lesik, L. Rondin, P. Spinicelli, O. Arcizet, J.-F. Roch, , and V. Jacques. Avoiding power broadening in optically detected magnetic resonance of single nv defects for enhanced dc magnetic field sensitivity. *PRB*, 84(195204), 2011.

[18] R. J. Epstein, F. M. Mendoza, Y. K. Kato, and D. D. Awschalom. Anisotropic interactions of a single spin and dark-spin spectroscopy in diamond. *Nat.Phys.*, 1, October 2005.

[19] J. S. Hodges, N. Y. Yao, D. Maclaurin, C. Rastogi, M. D. Lukin, and D. Englund. Timekeeping with electron spin states in diamond. *Phys. Rev. A*, 87(032118), March 2013.

[20] I.K. Kominis, T.W. Kornack, J.C. Allred, and M. Romalis. A subfemtotesla multichannel atomic magnetometer. *Nature*, 422, April 2003.

[21] G. Kucsko, P. C. Maurer, N. Y. Yao, M. Kubo, H. J. Noh, P. K. Lo, H. Park, and M. D. Lukin. Nanometre-scale thermometry in a living cell. *Nature*, 500:54, 2013.

[22] Linh My Pham. *Magnetic Field Sensing with Nitrogen-Vacancy Color Centers in Diamond.* PhD dissertation, Harvard University, Department of Applied Physics, May 2013.

[23] J. R. Rabeau, P. Reichart, G. Tamanyan, D. N. Jamieson, S. Prawer, F. Jelezko, T. Gaebel, I. Popa, M. Domhan, and J. Wrachtrup. Implantation of labelled single nitrogen vacancy centers in diamond using 15n. *App. Phys. Lett.*, 88(023113), 2006.

[24] B. Smeltzer, L. Childress, and A. Gali. 13c hyperfine interactions in the nitrogen-vacancy centre in diamond. *New J. Phys.*, 13(025021), 2011.

[25] T.M. Stace. Quantum limits of thermometry. *Phys. Rev. A*, 82(011611), 2010.

[26] D. M. Toyli, D. J. Christle, A. Alkauskas, B. B. Buckley, C. G. Van de Walle, and D. D. Awschalom. Measurement and control of single nitrogen-vacancy center spins above 600 k. *PRX*, 2(031001), July 2012.

[27] D. M. Toyli, C. F. de las Casasa, D. J. Christlea, V. V. Dobrovitskib, and D. D. Awschalom. Fluorescence thermometry enhanced by the quantum coherence of single spins in diamond. *PNAS*, 110(21), April 2013.